iScience

CellPress
OPEN ACCESS

Article

A study of cation-dependent inverse hydrogen bonds and magnetic exchange-couplings in lanthanacarborane complexes

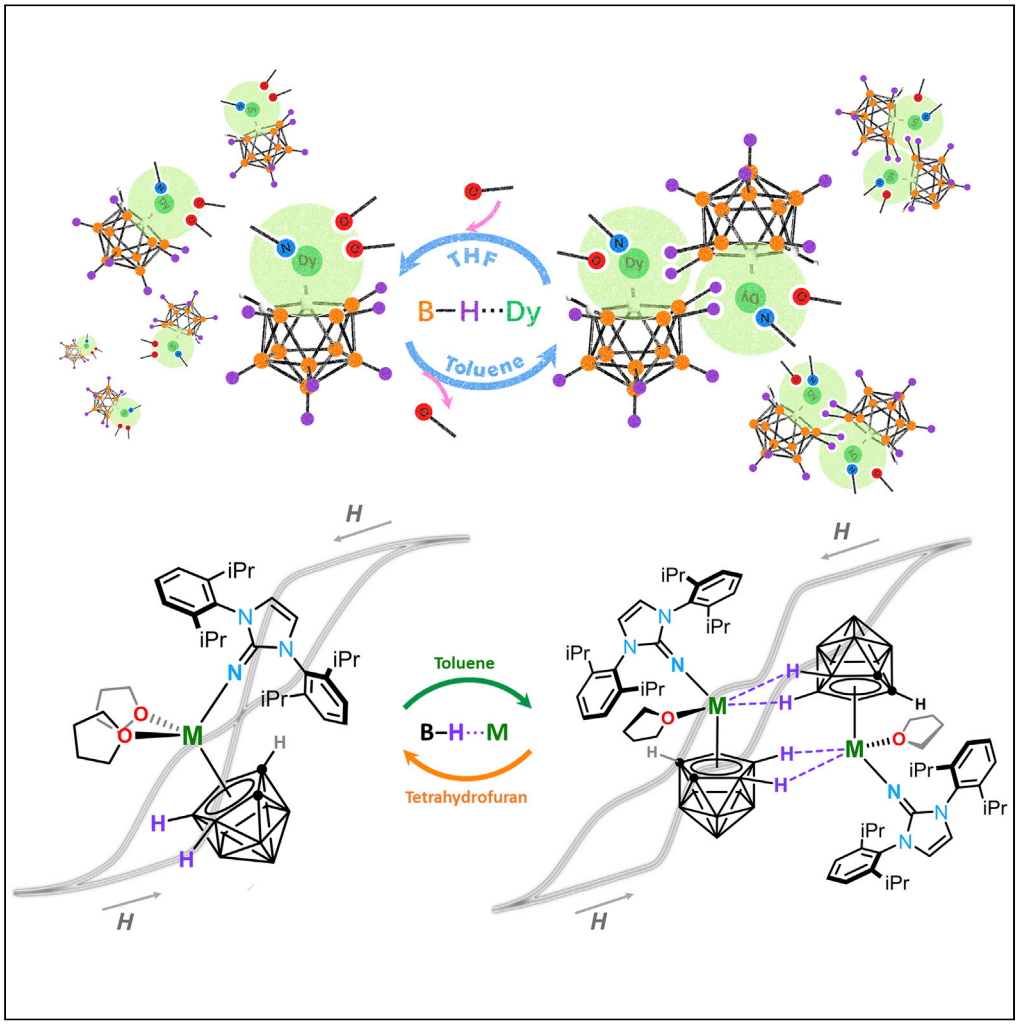

Peng-Bo Jin, Qian-Cheng Luo, Yuan-Qi Zhai, ..., Xu-Feng Zhang, Yi Lv, Yan-Zhen Zheng

zheng.yanzhen@xjtu.edu.cn

Highlights

Cation-dependent inverse hydrogen bonds are found in lanthanacarborane complexes

The lanthanacarborane dimeric assembly via inverse hydrogen bonds is reversible

The average bonding energy of $B-H^{\delta-}\cdots Ln^{3+}$ is larger than 24 kJ/mol

Inverse hydrogen bonded dysprosiacarborane dimers are single-molecule magnets

Jin et al., iScience 24, 102760
July 23, 2021
https://doi.org/10.1016/j.isci.2021.102760

iScience

CellPress
OPEN ACCESS

Article

A study of cation-dependent inverse hydrogen bonds and magnetic exchange-couplings in lanthanacarborane complexes

Peng-Bo Jin,[1,6] Qian-Cheng Luo,[1,6] Yuan-Qi Zhai,[1] Yi-Dian Wang,[1] Yan Ma,[1] Lei Tian,[2] Xinliang Zhang,[3] Chao Ke,[4] Xu-Feng Zhang,[5] Yi Lv,[5] and Yan-Zhen Zheng[1,7,*]

SUMMARY

Ten lanthanacarborane complexes were synthesized to study the rare $B-H^{\delta-}\cdots M^{n+}$ inverse hydrogen bonds (IHBs). The average bonding energy of $B-H^{\delta-}\cdots Ln^{3+}$ is theoretically determined to be larger than 24 kJ/mol, which is comparable to moderately strong hydrogen bonds (21–56 kJ/mol). In addition to NMR and IR, magnetometer was used to study the exchange-coupling interaction via such $B-H^{\delta-}\cdots Ln^{3+}$ IHBs in detail, and the coupling constant is determined to be $-2.0\ cm^{-1}$, which is strong enough to compare with single-atom bridged dysprosium(III) complexes. Two imidazolin-iminato incorporated complexes have shown energy barrier for magnetization reversal larger than 1000 K, and the exchange-biasing effects are evident. Moreover, the bonding strengths of $B-H^{\delta-}\cdots M^{n+}$ IHBs are cation-dependent. If M = Na, the $B-H^{\delta-}\cdots Na^{+}$ bonding energy is reduced to 14 kJ/mol, and the dimerization process is no longer reversible. The exchange-biasing effect is also disappeared. We believe such a finding extends our knowledge of IHBs.

INTRODUCTION

Hydrogen bond (HB) is a fundamental supramolecular interaction underpinning the complicated processes of self-assembly, molecular recognition, crystal engineering, material chemistry, catalytic cycle, and biological function (Steiner, 2002; Hannon, 2007; Braga, et al., 1999). Typical HB takes the form of $X-H^{\delta+}\cdots Y$ comprising a positively charged hydrogen atom between a pair of other electron donor-acceptor atoms (Scheme 1a). Interestingly, the bonding energy of HB varies widely, mostly depending on the electron affinity of two other atoms and the geometry among these three atoms (Rodham, et al., 1993). For instance, the bonding energy of weak C–H···F HB is about 0.8 kJ mol^{-1} (Howard, et al., 1996); for a typical water dimer, the bonding energy of O–H···O HB is about 21 kJ mol^{-1} (Gu, et al., 1999); while for linear bifluoride anion, the bonding energy of F–H···F HB can go up to 161 kJ mol^{-1} (Gronert, 1993). In some special cases, such as the dihydrogen bonds (Scheme 1b), the role of the H atom is divided — one H atom accepts the electrons from the other (Liu and Hoffmann, 1995).

If the hydrogen atom acts as the electronic donor, such as the case shown in Scheme 1c, this type of $X-H^{\delta-}\cdots Y$ HB can be called as an inverse hydrogen bond (IHB) because the hydrogen atom is negatively charged and acts as an electron donor. IHB was initially proposed by Rozas et al., in 1997 when investigating the intermolecular interactions in metal hydrides due to the electronegativity of the hydrogen atom is much stronger than many metal atoms (Rozas, et al., 1997). Later, the IHBs were also found in nonmetal hydrides, such as SiH_4 and XeH_2 (Blanco et al., 2008; Yuan, et al., 2011). But as a whole, IHBs are still very scarce due to lower electron affinity of the hydrogen atom in most of the X-H bonds.

As boron atom is electron deficit, the electron tends to polarize to the hydrogen atom with a formal form of $B^{\delta+}-H^{\delta-}$ (Pauling, 1960). This is widely observed in boron clusters (Núñez, et al., 2016) and carbon-boron clusters (carborane) (Hosmane, 2011; Zhao and Xie, 2016). Such boron-based clusters are found to be able to form $B^{\delta+}-H^{\delta-}\cdots H^{\delta+}-C^{\delta-}$ dihydrogen bond (Cui et al., 2020; Xing et al., 2020) or $B^{\delta+}-H^{\delta-}\cdots M^{n+}$ interactions (Hewes, et al., 1984; Baker, et al., 1978; Behnken, et al., 1985; Axtell, et al., 2016) when coordinating metal centers (Silva and Hardie, 2012). For M = lanthanide, several polymetallic lanthanacarborane

[1]Frontier Institute of Science and Technology (FIST), Xi'an Jiaotong University Shenzhen Research School, State Key Laboratory for Mechanical Behavior of Materials, MOE Key Laboratory for Nonequilibrium Synthesis and Modulation of Condensed Matter and School of Chemistry, Xi'an Jiaotong University, 99 Yanxiang Road, Xi'an, Shaanxi, P.R. China

[2]State Key Laboratory of Military Stomatology, National Clinical Research Center of Oral Diseases, Shaanxi Key Laboratory of Oral Diseases, Department of Cranio-facial Trauma and Orthognathic Surgery, School of Stomatology, The Fourth Military Medical University, Xi'an, No. 145, Changle Xi Road, 710032 Xi'an, Shaanxi, P.R. China

[3]Department of Spine Surgery, Honghui Hospital, Xi'an Jiaotong University, 710054 Xi'an, Shaanxi, P.R. China

[4]Department of Orthopaedic Trauma, Honghui Hospital, College of Medicine, Xi'an Jiaotong University, 710054 Xi'an, Shaanxi, P.R. China

[5]Department of Hepatobiliary Surgery, The First Affiliated Hospital of Xi'an Jiaotong University, 277 West Yanta Road, 710061 Xi'an, Shaanxi, P.R. China

[6]These authors contributed equally

[7]Lead contact

*Correspondence: zheng.yanzhen@xjtu.edu.cn

https://doi.org/10.1016/j.isci.2021.102760

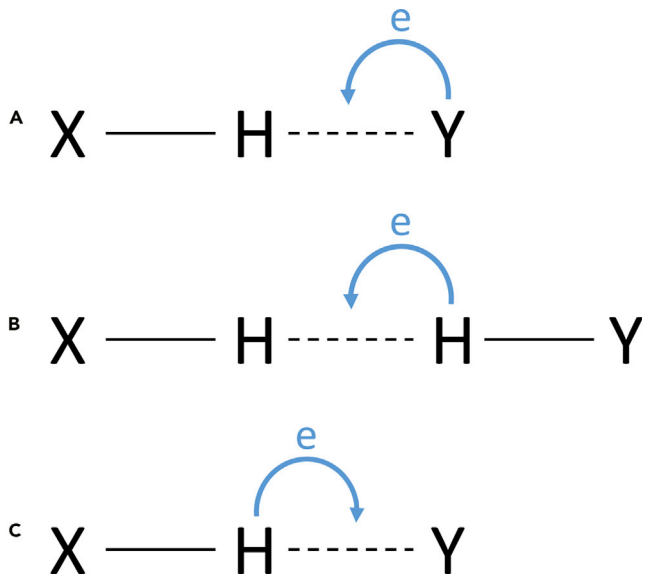

Scheme 1. Three kinds of hydrogen bonds

systems bridged with $B^{\delta+}-H^{\delta-}\cdots Ln^{3+}$ IHBs were reported previously, showing interesting and diversified structural motifs (Xie, et al., 1999; Cheung, et al., 2005; Wang, et al., 2003). However, the bonding energy was believed to be very weak due to the internal 4f orbitals of the lanthanide ions. Moreover, their physical properties are barely studied despite that dysprosiacarboranes are recently confirmed to be milestone entities for single-molecule magnets (SMMs) (Jin, et al., 2020), which may have potential applications in high-density information storage, spintronic devices, and quantum information processing, and so on (Gatteschi, et al., 2006; Mannini, et al., 2009; Leuenberger and Loss, 2001; Bogani and Wernsdorfer, 2008). In addition, the magnetic exchange coupling transferred by $B^{\delta+}-H^{\delta-}\cdots Ln^{3+}$ IHBs is less studied although the magnetic properties affected by HBs have been discussed in some cases (Gupta et al., 2016a; 2016b; Norre, et al., 2020; Canaj, et al., 2018).

Herein, we utilize 1,3-bis(2,6-diisopropylphenyl)-imidazolin-2-iminato ($Im^{Dipp}N^{-}$) and 2,6-bis(diphenylmethyl)-4-methylphenol (HOAr*) to construct ten lanthanacarborane complexes. The $Im^{Dipp}N^{-}$-based dimers namely [*closo-nido*-(η^5-$C_2B_9H_9$) (μ-H_2)M($Im^{Dipp}N$) (THF)]$_2$ (M = Dy, **2Dy**; M = Y, **2Y**) and [*exo-nido*-(μ-H_4-*o*-xylylene-$C_2B_9H_9$)Dy($Im^{Dipp}N$) (THF)]$_2$ **4Dy** are assembled from three respective monomeric precursors, [*closo-nido*-(η^5-$C_2B_9H_{11}$)M($Im^{Dipp}N$) (THF)$_2$], (M = Dy **1Dy**; M = Y, **1Y**), and [*closo-nido*-(η^5-*o*-xylylene-$C_2B_9H_9$)Dy($Im^{Dipp}N$) (THF)$_2$] **3Dy**. We found the bonding energies of $B-H^{\delta-}\cdots Ln^{3+}$ IHBs in the dimeric complexes are larger than 24 kJ/mol, which are strong enough to construct the exchange biasing SMMs (Wernsdorfer, et al., 2002; Nava, et al., 2015; Nguyen, et al., 2016) with enhanced hysteresis loops and energy barriers (U_{eff}) for magnetization reversal.

More importantly, we found the bonding strength of $B-H^{\delta-}\cdots M^{n+}$ is cation-dependent. If the trivalent lanthanide is changed to the sodium(I) cation, the $B-H^{\delta-}\cdots Na^{+}$ interaction is much weakened (bonding energy of $B-H^{\delta-}\cdots Na^{+}$ is determined to be 15 kJ/mol). This is well demonstrated in two phenol-substituted dimeric derivatives [*closo-nido*-(OAr*)M(THF) (η^5-Et_2-$C_2B_9H_6$)Cl(μ-H)$_3$Na(THF)$_2$]$_2$ (M = Dy, **6Dy**; M = Y, **6Y**) which are respectively assembled from the monomers [*exo-nido*-(OAr*)M(THF)$_2$(η^3-Et_2-$C_2B_9H_6$)Cl][(μ-H)$_3$Na(THF)$_3$] (M = Dy, **5Dy**; M = Y, **5Y**). The reduced bonding strengths of these complexes are well reflected in their disappeared exchange-biasing effects (for details, see below).

RESULTS AND DISCUSSION

Synthesis

As shown in Figure 1A, the lanthanacarborane dimers (**2Dy**, **2Y**, and **4Dy**) are generated from the assembly of monomers of **1Dy**, **1Y** and **3Dy**, respectively. The monomers **1Dy**, **1Y,** and **3Dy** are generated from salt metathesis reaction between [($Im^{Dipp}N$)MCl_2(THF)$_3$] (M = Dy, Y) and dicarbollide ligands *nido*-[$C_2B_9H_{11}$]

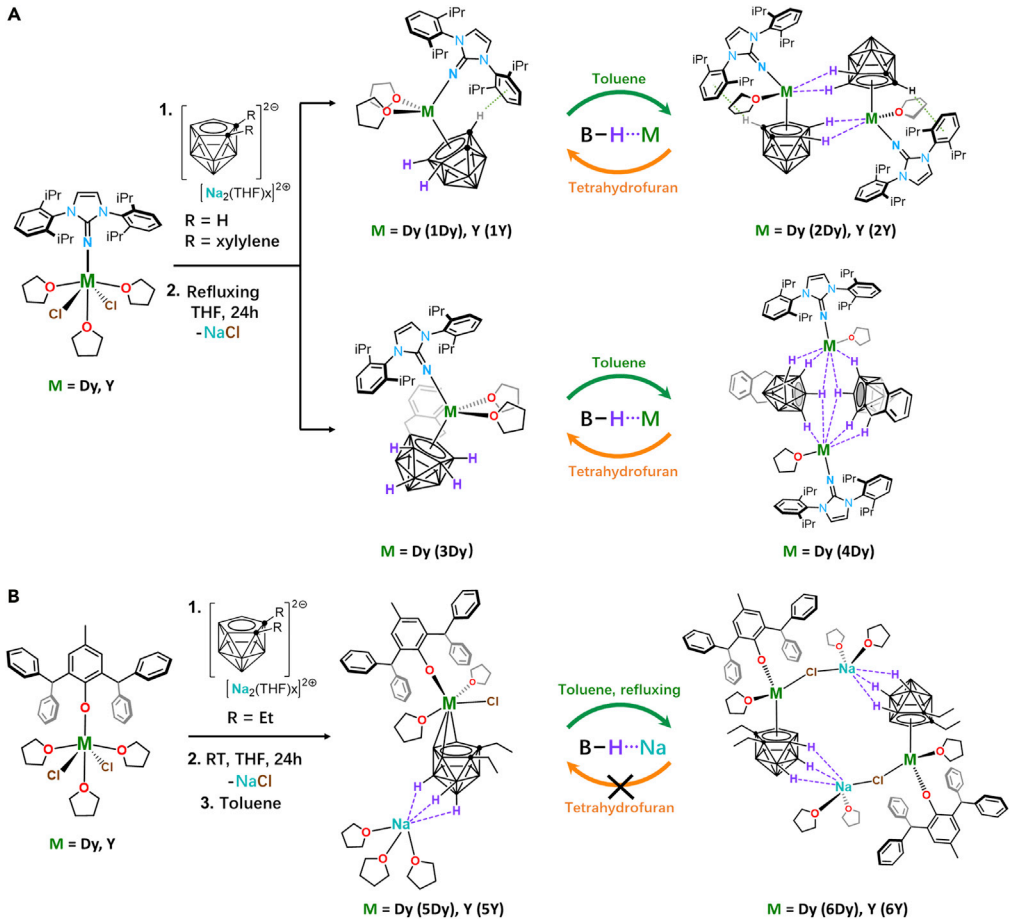

Figure 1. The schematic diagram of the synthetic routes

(A) The synthetic routes to the imidazolin-iminato incorporated complexes **1Dy**, **1Y**, **2Dy**, **2Y**, **3Dy**, and **4Dy** and the reversible transformations between monomers (**1Dy**, **1Y** and **3Dy**) and dimers (**2Dy**, **2Y**, and **4Dy**).

(B) The synthetic routes to the phenol derivative incorporated complexes **5Dy**, **5Y**, **6Dy**, and **6Y**.

$[Na]_2$ and *nido*-[*o*-xylylene-$C_2B_9H_9$][$Na]_2$ ([{*o*-$C_6H_4(CH_2)_2$}$C_2B_9H_9$][$Na]_2$), respectively. Analogous to the synthesis of the above mentioned imidazolin-iminato incorporated lanthanacarboranes, the phenol derivative ligands OAr^{*-} were introduced as well to have a better comparison with $Im^{Dipp}N^-$. As showed in Figure 1B, bottom, a salt metathesis reaction between [Na_2][*o*-Et_2-$C_2B_9H_9$] and the dichlorides [(OAr*)$MCl_2(THF)_3$] (M = Dy, Y) in THF solution produces **5Dy** and its yttrium derivative **5Y**. Moreover, complexes **5Dy** and **5Y** serve as intermediates further linking with each other to produce dinuclear structures **6Dy** and **6Y**. Supramolecular interaction between $B-H^{\delta-}$ and Ln^{3+} is verified via the reversible transformation processes of dimers (**2Dy** and **4Dy**) and monomers (**1Dy** and **3Dy**) under different solvent condition. However, monomers **5** cannot be reversibly isolated by simply treating dimers **6** with THF, which is different from the imidazolin-iminato incorporated complexes.

Structures

Single crystal X-ray diffraction measurement reveals the similar connectivity between the monomers and the dimers. Moreover, the yttrium(III) and dysprosium(III) complexes are isomorphous, so below we take the dysprosium(III) analog to discuss as a representative. Compounds **1Dy**, **2Dy**, and **3Dy** crystallized in monoclinic space group $P2_1/c$, while **4Dy**, 5**Dy** ,and **6Dy** are in *P*-1.

For **1Dy**, the pentagonal C_2B_3 bonding face of the dicarbollide ligand is η^5-bound to the Dy(III) center and the Dy···B/C distances to the η^5-$C_2B_3^{2-}$ face are ranging from 2.623(5) to 2.667(4) Å, while the $Im^{Dipp}N^-$

ligand links to Dy(III) in an almost linear fashion (C–N–Dy angle of 176.05°) with a very short Dy–N bond of 2.095(3) Å (Figure S1). In addition to the $C_2B_9H_{11}^{2-}$and $Im^{Dipp}N^-$ ligands, the coordination sphere of Dy(III) center is completed by two THFs to give a tetrahedral geometry with Dy–O bond length at around 2.36 Å.

For **2Dy** (Figure S3), the two asymmetric units connect to each other via four B–$H^{\delta-}\cdots Dy^{3+}$ IHBs with the distance of $Dy^{3+}\cdots Dy^{3+}$ of 4.081 Å. The angles of B–H···Dy are ranging from 96.43° to 109.44°, and the H···Dy distances are between 2.25 and 2.46 Å. In contrast to **1Dy**, one THF molecule is eliminated. The Dy–O distance remains unchanged, while the Dy–N bond is a bit lengthened, to 2.107(3) Å. The bending angle of N–Dy–centroid (C_2B_3) is 117.27° and the Dy-centroid (C_2B_3) distance is 2.343 Å, similar to these of **1Dy**.

The larger substituent group [*o*-xylylene-$C_2B_9H_9]^{2-}$ results in the monomeric compound **3Dy** (Figure S5), which has a wider bending angle N–Dy–centroid of 131.37° and a very short Dy–N bond of 2.123(3) Å. The Dy···B/C distances to the η^5-$C_2B_3^{2-}$ face have a wider range of 2.601(4) to 2.788(3) Å and a much shorted Dy··· centroid (C_2B_3) distance of 2.275 Å.

However, due to the steric hindrance of [*o*-xylylene-$C_2B_9H_9]^{2-}$ ligands the Dy^{3+} in **4Dy** is no longer half sandwiched. Rather, it forms a pair of centrosymmetric *exo-nido*-dysprosiacarborane bridges (Figure S7). The Dy^{3+} ions are bridged by multiple B–$H^{\delta-}\cdots Dy^{3+}$ IHBs with $Dy^{3+}\cdots Dy^{3+}$ distance of 4.162 Å, among which the H1 atom is from the lower belt of the dicarbollide cage and other hydrogen atoms (H2, H3, and H4) are from the C_2B_3 pentagonal face. The distances of H–Dy range from 2.307 Å to 2.572 Å and the angles of B–H···Dy range from 88.87° to 100.01°. Remarkably, the Dy–N bond length reduces to 2.066(2) Å, which is the shortest among these structures. This is probably due to the edge-coordinate mode of the dicarbollide ligand which less diverges the electrostatic attraction from the central cation.

For **5Dy** (Figure S9), the Dy^{3+} ion has a slip distortion from the center of the C_2B_3 bonding face of the carboranyl ligand, which leads to much longer Dy–C(cage) and shorter Dy–B(cage) distances than that of **1Dy** and **3Dy**. The shortest Dy–C bond is 3.155(2) Å and Dy–B distances are ranging from 2.570(3) Å to 2.868(4) Å. The Dy(III) ion is bound to the $(C_2H_5)_2C_2B_9H_9^{2-}$ ligand with η^3 fashion. The Dy–$O_{(PhO)}$ bond length is 2.112(2) Å, much shorter than the Dy–$O_{(THF)}$ (2.432(3) Å and 2.455(2) Å). The solvated Na(I) ion is chelated by the carboranyl cages via triple B–H···Na^+ interactions and the H···Na^+ distances are between 2.601 and 2.724 Å, which are much longer than those of H···M^{3+} in **1**-**4**, indicative weaker IHBs.

For **6Dy** (Figure S11), the Na(I) cation attaches to the chloride by electrostatic force with ionic bond length of 2.738(3) Å. The Na–Cl ionic bonds connect two adjacent units to produce a pair of centrosymmetric *closo-nido*-dysprosiacarborane bridges. Thus, the two Dy(III) centers in **6Dy** are away from each other with $Dy^{3+}\cdots Dy^{3+}$ distance of 6.907 Å. Each Dy(III) ion in **6Dy** has the similar coordination environment as those in **5Dy** except for shorter H···Na distances (2.356–2.659 Å). The Dy to the B/C of the η^5-$C_2B_3^{2-}$ face distances are ranging from 2.657(6) Å to 2.726(5) Å, and the $Dy^{3+}\cdots C_2B_3^{2-}$ face centroid distance is 2.268 Å. Other coordination sites were occupied by the oxygen atom of the $[OAr^*]^-$ ligand and a Cl^- with Dy–$O_{(PhO)}$ and Dy–Cl distances of 2.098(4) Å and 2.626(3) Å, respectively. Note that the Dy–$O_{(PhO)}$ distance of **6Dy** is shorter than that (2.112(2) Å) of **5Dy**.

The crystal packing diagrams along *a* axis of **1Dy** to **6Dy** are shown in Figures S1–S12, respectively. The Dy(III) centers of different molecules are away from each other with the shortest intermolecular $Dy^{3+}\cdots Dy^{3+}$ distance 9.47 Å in **3Dy** and the longest 12.48 Å in **6Dy**.

NMR and IR spectra

As the Y(III) is diamagnetic high-resolution ^{1}H NMR and ^{11}B NMR spectra can be obtained to study the strength of the B–$H^{\delta-}\cdots M^{3+}$ interaction (Figure 2A). These interactions can be well detected by the significant difference of the chemical shifts of **1Y** in THF-d_8 and **2Y** in Benzene-d_6. Besides, the signals of the alkyl hydrogen atoms of **2Y** have the upfield shifts (a, b, c, d, f, g, h) while B-H broad signal (i) shifts downfield (from −2.6 ~ −3.5 ppm to −1.8 ~ −2.5 ppm) comparing with **1Y**, which is attributed to the positive charge environment (Y^{3+}) of B–$H^{\delta-}\cdots Y^{3+}$ linkages. In contrast, the transition from complexes **5Y** to **6Y** makes no difference to their chemical environment, giving very similar ^{1}H NMR spectrums and almost identical B-H signals in the range of −1.3 ~ −2.0 ppm (Figures S13 and S14). Moreover, for the dinuclear complex **2Y**, the alkyl hydrogen atoms of two coordinated imidazolin-iminato ligands have non-equivalent chemical

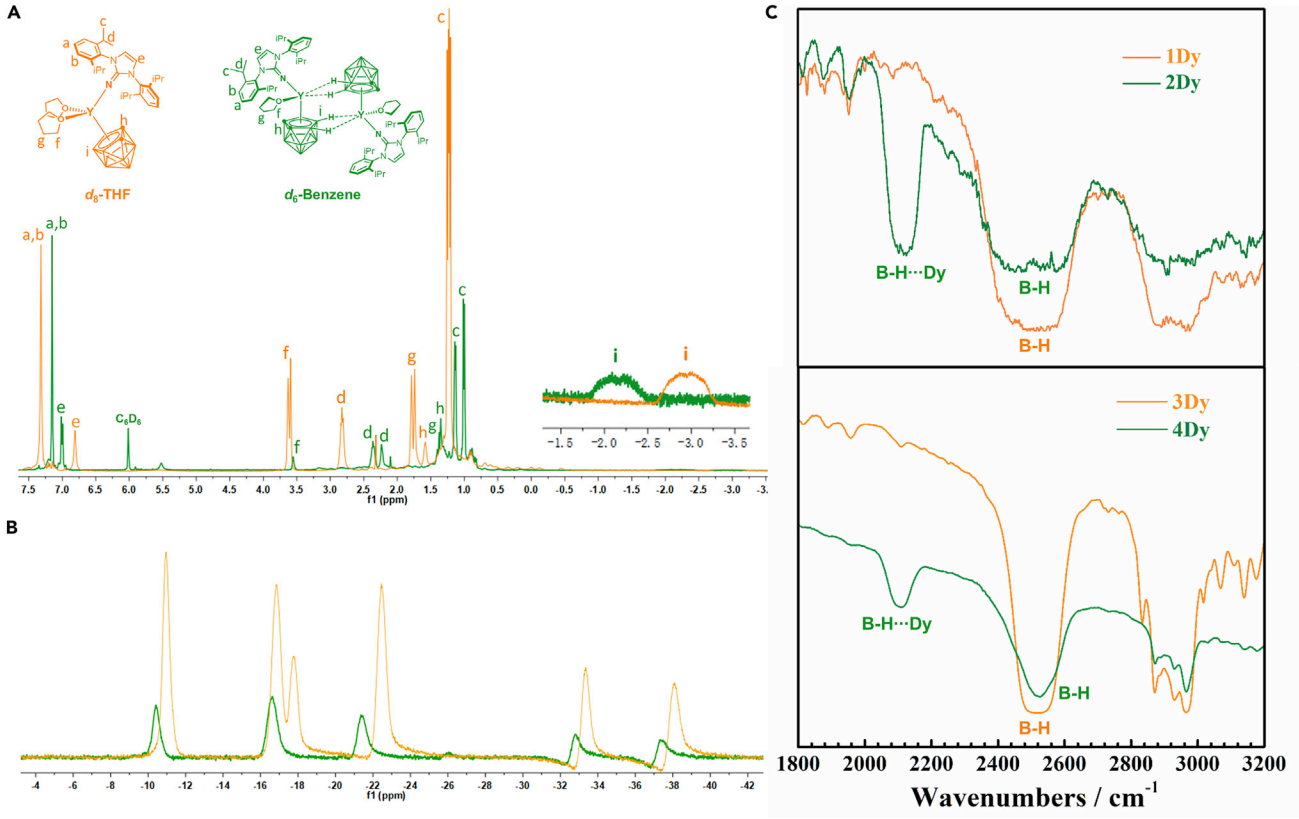

Figure 2. The NMR and Infrared spectrums

(A and B) The ^{1}H NMR (A) and ^{11}B NMR (B) spectrum assignment for complexes **1Y** (orange) and **2Y** (olive-green). (Insert) Expanded view of the chemical shift from −3.5 to −1.5 ppm.

(C) Infrared spectrum of complexes **1Dy** and **3Dy** (orange) and **2Y** and **4Dy** (olive-green).

environment and are with slightly difference to give the separated C−H signals (e d and c). The smaller number of coordinated THF molecules in **2Y** are also well detected with much weaker corresponding signals (f and g). The ^{11}B NMR shows the six resonances with 2:2:1:2:1:1 ratio from −10 to −40 ppm for **1Y** and five resonances with 2:3:2:1:1 ratio for **2Y**, whose signals shift downfield (Figure 2B). Most of peaks of monomer **1Y** and dimer **2Y** are asymmetrical except the two in −37.2 and −32.6 ppm of **2Y**, giving the symmetric peaks which is mainly due to the existence of quadruple B−H$^{\delta-}$···Y^{3+} interactions in **2Y**.

Solid-state infrared (IR) spectra of **1** to **6** exhibit broad resonance region at 2500 cm^{-1}, which is the characteristic peak of B−H stretches from carboranyl cages (Figures 2C and S17−S22). This is also a quick way to identify the existence of carboranyl ligands. Besides, an additional strong absorption is observed in ~2100 cm^{-1} for **2Dy**, **2Y,** and **4Dy** but not for **1Dy**, **1Y,** and **3Dy** (Figures S17 and S18), which is suggestive of the existence of B−H$^{\delta-}$···M^{3+} stretching bands in **2Dy**, **2Y,** and **4Dy**. Such M···μ-H−B interactions have been noted previously (Chui, et al., 2000). In contrast, the IR spectra of complexes **5** and **6** give no extra B−H stretching peaks even at the presence of triple B−H$^{\delta-}$···Na^{+} interactions (Figures S19−S22), indicative of much weaker IHBs.

Computational studies

Density Function Theory (DFT) calculation was employed to acquire specific bonding energy for B−H$^{\delta-}$···Dy^{3+} and B−H$^{\delta-}$···Na^{+} IHBs using Gaussian 09. The B−H$^{\delta-}$ surface with negative electrostatic potential has strong interaction to Dy^{3+} (Figure 3A). The average bonding energy (BE$_{avg}$) is introduced by considering the complexes' centrosymmetry and similarity of Dy−H and Na−H distances. The calculation gives BE$_{avg(B-H\cdots Dy)}$ = −33.75 kJ/mol for **2Dy**, BE$_{avg(B-H\cdots Dy)}$ = −24.99 KJ/mol for **4Dy**, and BE$_{avg(B-H\cdots Na)}$ = −14.62 KJ/mol for **6Dy** (Figures 3B, 3C, and S77). The striking contrast of the binding

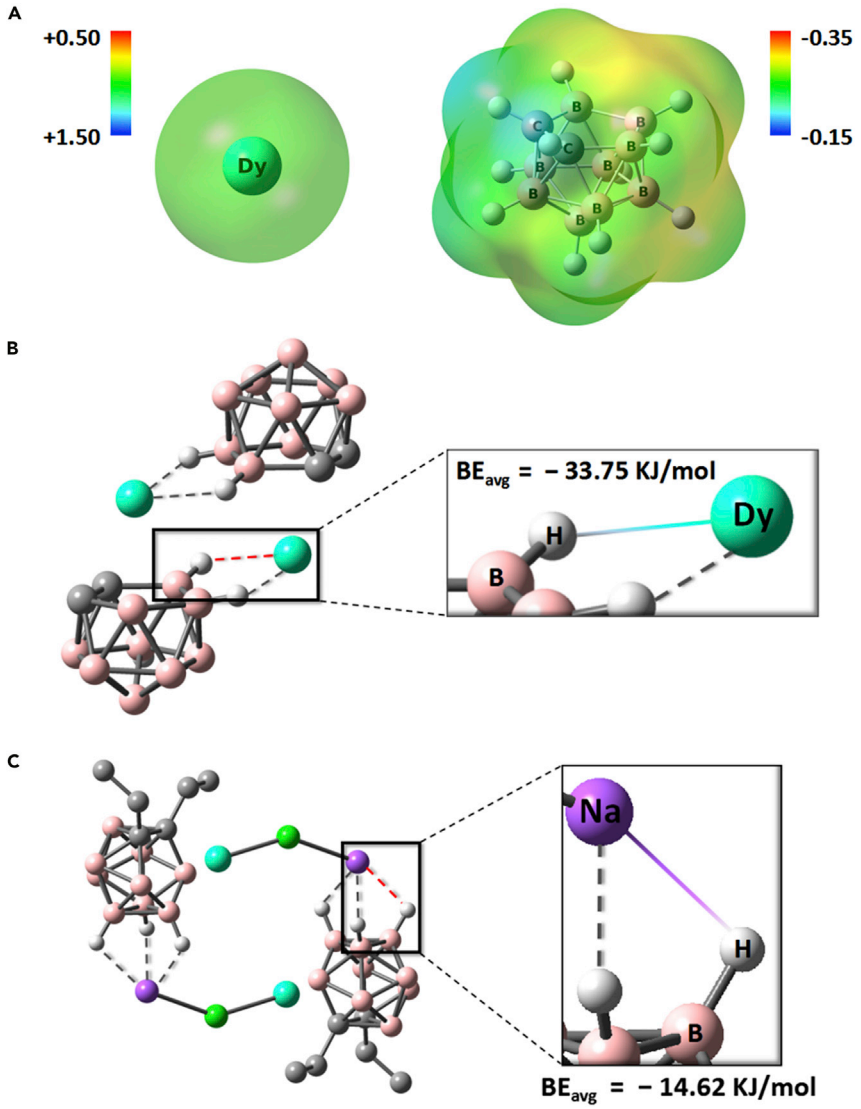

Figure 3. Density Function Theory (DFT) calculation

(A) Electrostatic potentials of Dy(III) and *nido*-$[C_2B_9H_{11}]^{2-}$ ((isovalue = 0.001)).

(B and C) Bonding energy between fragments for **2Dy** (B) and **6Dy**'s (C) model complexes through DFT calculation. For clarity, certain hydrogen atoms in both complexes are omitted. (cyan for Dy, pink for B, gray for C, green for Cl, purple for Na and white for H).

energy between $B-H^{\delta-}\cdots Dy^{3+}$ and $B-H^{\delta-}\cdots Na^{+}$ is attributed to the cation dependent electrostatic interactions and exist one kind of relationship as $BE_{avg(B-H\cdots Dy)} > BE_{avg(B-H\cdots Na)}$. Nevertheless, these energy range is comparable to other hydrogen-bonded complexes which show $B–H\cdots\pi$ interactions with the binding energy ranging from −16.47 to −21.19 kJ/mol by using natural population analysis (Kolandaivel and Nirmala, 2004; Zhang, et al., 2016). Moreover, to confirm the strength relationship of $B-H^{\delta-}\cdots Dy^{3+}$ and $B-H^{\delta-}\cdots Na^{+}$, atoms in molecules (AIM) was adopted by using Multiwfn, which is a popular theory on electron density (ED) topological analysis (Bader, 1994; Lu and Chen, 2012a, 2012b). In this theory, the point of zero ED gradient in space is called critical point (CP), primarily consisting of four sorts: (3,-3), (3,-1), (3,+1), and (3,+3). Among them, the (3, −1) point, the second order saddle point of the ED function, is usually located between both adjacent atoms, called bond critical point (BCP) whose ED value can be employed to measure the strength of the same variety of interactions. Here for simplicity, these dimer molecules used in AIM analysis are the same as model dimer complexes in DFT calculations. All BCPs around $B-H^{\delta-}\cdots M^{n+}$ were found and their calculated total ED was listed in Table S40. Similarly, we

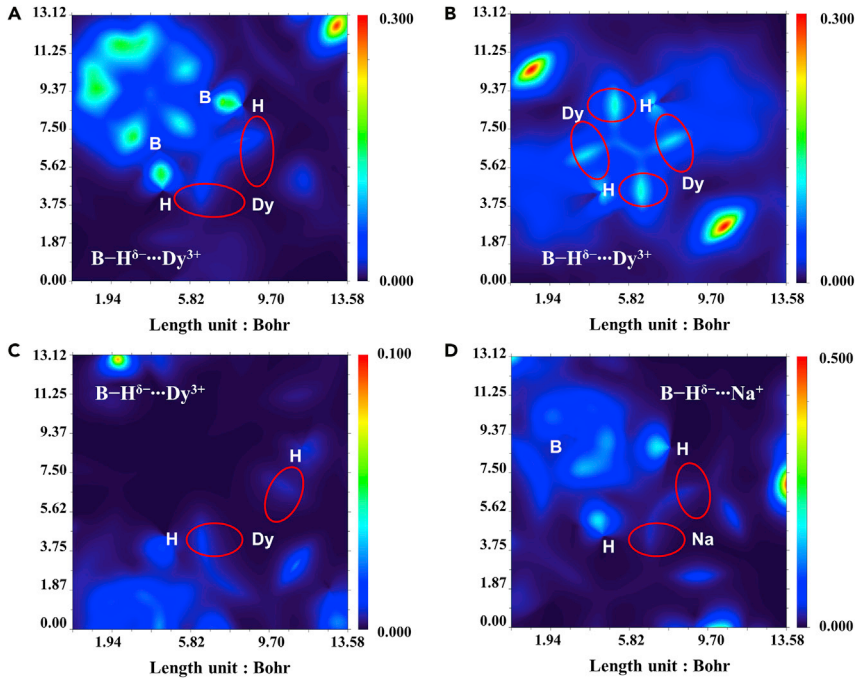

Figure 4. Cross section coloring maps
B–H$^{\delta-}$···Dy^{3+} and B–H$^{\delta-}$···Na^{+} interactions in **2Dy** (A), **4Dy** (B, C), and **6Dy** (D) respectively.

introduced the average value of ED, named ρ_{avg}. It is evident that there is such a relationship: ρ_{avg}(**2Dy**) ≈ ρ_{avg}(**4Dy**) > ρ_{avg}(**6Dy**), which is consistent with the strength relation of calculated IHB binding energy, indicating the reliability of DFT calculations.

Intermolecular interaction region and its characteristics can be exhibited using Independent Gradient Model (IGM), which is a methodology based on ED (Lefebvre, et al., 2017). Generally, the gradients of ED between both atoms with interaction possess contrary signs. When the total gradient superposed in the region is zero, the position is exactly right BCP. Under normal circumstances, the total gradient at a certain point is regarded as the sum of the atomic gradients, denoted as $|\nabla\rho|$, while the IGM type density gradient ($|\nabla\rho^{IGM}|$) is defined as the sum of the absolute values of the individual atomic gradient. The so-called δg function is the difference between the above two quantities, as shown in Equation 1. The absolute value is introduced in calculation, thus the value of the function between both atoms, especially at BCP, is not relatively small, leading to the fact that the magnitude of δg is proportional to the strength of interactions and also outlines bonding regions between both atoms. To reveal distribution character of δg function, variable sections from their 3D isosurface representations based on this model have been plotted, showing existing B–H$^{\delta-}$···Dy^{3+} and B–H$^{\delta-}$···Na^{+} interactions in complexes **2Dy**, **4Dy,** and **6Dy** using Multiwfn (Figure 4). For clarity, we adjusted the upper limits of δg function in these plots and the color from red to blue corresponds to the descending δg value. The part of each plot circled in red illustrates the existence of the B–H$^{\delta-}$···M^{n+}. Compared with other regions, these interactions are evidently weaker than covalent bond.

$$\delta g = \left|\nabla\rho^{IGM}\right| - |\nabla\rho| \qquad \text{(Equation 1)}$$

Moreover, fingerprint plots and color-mapped isosurface graphs of Hirshfeld surface were produced by using Multiwfn and VMD (Figure S78) (Spackman and Jayatilakaa, 2009; Lu and Chen, 2012a; 2012b; Humphrey, et al., 1996). As we considered two Dy(III) (**2Dy** and **4Dy**) and one Na(I) (**6Dy**) ion in the central area, the spikes at bottom of the finger plots mean existence of interactions between Dy(III) or Na(I) and other coordinated atoms in the peripheral areas. Meanwhile, the color from blue to red corresponds to ED varying from 0.0 to 0.015 a.u. in color-mapped isosurface graphs of Hirshfeld surface, indicating that red color area represents relatively large ED. All types of plots are in good agreement with X-ray diffraction analysis and DFT calculations, further proving that the interaction caused by boron-hydrogen bridging is

crucial to the formation of binuclear compounds from mononuclear compounds in our system. At this point, we may conclude that there are two main advantages to form this kind of infrequent bonding interaction in our system: (1) the dual role of THF—reactant and solvent: abundant toluene goes against the coordination between THF and Dy(III); (2) more positive electrostatic potential of Dy(III) benefits the formation of $B-H^{\delta-}\cdots Dy^{3+}$ interaction.

Magnetic exchange-coupling interactions

For better understanding the exchange couplings transferred by $B-H^{\delta-}\cdots M^{3+}$ interactions between Ln^{3+} centers, we thoroughly investigate the magnetic properties of dysprosium(III)-based dinuclear complexes **2Dy**, **4Dy,** and **6Dy**. Such couplings can be displayed in the field- and temperature-dependent magnetization (*M*) plots. The temperature-dependent molar magnetic susceptibilities (χ_m) under an applied field of 1000 Oe over the temperature range 2 K–300 K give the room temperature $\chi_m T$ products (in emu K mol^{-1} and the same below) to be 27.48, 27.51, and 27.73 for **2Dy**, **4Dy** and **6Dy**, respectively. These values are slightly below two free Dy(III) ions of 28.34 emu K mol^{-1} calculated from $S = 5/2$, $L = 5$, and $g = 4/3$ (Figures S23–S27). For **2Dy** and **4Dy**, the $\chi_m T$ curves decrease slowly from 300 K to 30 K and rapidly afterward (Figures S24 and S26). In contrast, the decreasing trend in **6Dy** is much slower largely due to the weaker interactions (Figure S27).

The effect of magnetic interaction is evident in the hysteresis loops (Figures 5 and S28–S33). For the monomers, namely complexes **1Dy**, **3Dy** and **5Dy**, the hysteresis loops are waist-restricted with strong quantum tunneling of magnetization (QTM) effect at zero field. In contrast, the loops remain opened around zero field for dimers, namely complexes **2Dy**, **4Dy,** and **6Dy**. Especially for **2Dy** and **4Dy**, in which the Dy(III) ions are bridged by $B-H^{\delta-}\cdots Dy^{3+}$ IHBs the coercive fields (H_c) are larger than 1000 Oe (Figure 5, top and S32, left); while for **6Dy**, in which the Dy^{3+} ions are separated without $B-H^{\delta-}\cdots Dy^{3+}$ linkage gives much smaller H_c of 600 Oe (Figure S32, right). Interestingly, step-like hysteresis loop is clearly observed for **2Dy** (Figure S28B). These steps are attributed to the level-crossing between the low-lying states of the dimer. If this complex is diluted with the yttrium(III) analog **2Y**, the formed diluted sample **2Dy@2Y** shows again waist-restricted shape (Figure S29, left), indicating the effect of intramolecular $Dy^{3+}\cdots Dy^{3+}$ interactions are absent.

The QTM step-like hysteresis loop of **2Dy** can also be well characterized with easy axis of single crystal sample (Figure 6, top, green), which is well explained with the Zeeman diagram of **2Dy** (Figure 6, bottom). Upon decreasing the field, the saturated magnetic moment gradually flips from the |− −> configuration of the ferromagnetic state to the antiferromagnetic states (|+ −>, |− +>). When it comes to 0.2 T, about 40% moments undergo a transition due to the QTM process at the field of level crossing between the (|− −>) and the (|+ −>, |− +>) states. At field values away from the avoided level crossing, the dimer states are approximately frozen by the significant magnetic anisotropy barrier, demonstrated with plateaus in the hysteresis loop. The plateaus last until the next tunneling happens at −0.2 T from antiferromagnetic states (|+ −>, |− +>) to ferromagnetic state (|+ +>). The single crystal sample of 5% diluted **2Dy@2Y** gives strong QTM at zero field, indicating the consequence of the absence of intra- and inter-molecular interactions (Figure 6, top, gray).

To further understand the exchange biasing phenomenon in **2Dy**, the intramolecular interaction between magnetic centers was studied through experimental data analysis and theoretical calculation. It has become a consensus that total interaction within both Dy(III) ion centers (J_{total}) primarily consist of magnetic exchange and dipole-dipole exchange whose coupling constants are expressed by J_{exch} and J_{dip}, respectively. Equation 2 is the Hamiltonian that expresses the relationship among the three coupling constants through $J_{total} = J_{exch} + J_{dip}$.

$$\widehat{H} = \widehat{H}_{exch} + \widehat{H}_{dip} = -J_{total}\widehat{\tilde{S}}_{1z}\widehat{\tilde{S}}_{2z} = -\left(J_{exch}\widehat{\tilde{S}}_{1z}\widehat{\tilde{S}}_{2z} + J_{dip}\widehat{\tilde{S}}_{1z}\widehat{\tilde{S}}_{2z}\right) \quad \text{(Equation 2)}$$

$$\overline{J}_{dip} = \frac{\mu_B{}^2}{|r|^3}\left[\overline{g}_1 \cdot \overline{g}_2 - 3\left(\overline{g}_1 \cdot \vec{r}\right)\left(\vec{r} \cdot \overline{g}_2\right)\right] \quad \text{(Equation 3)}$$

Equation 3 is the expression for dipole-dipole interaction. By using the POLY_ANISO module, the magnetic data can be fitted (Figures S24, S26, and S27). Based on J_{xx}, J_{yy}, and J_{zz}, this module also outputs the Zeeman diagrams in three directions (Figure S76). As shown in Table 1, the magnitude of the *J* values is indicative of the strength of magnetic interactions and the sign of the *J* values represent ferro (+) and

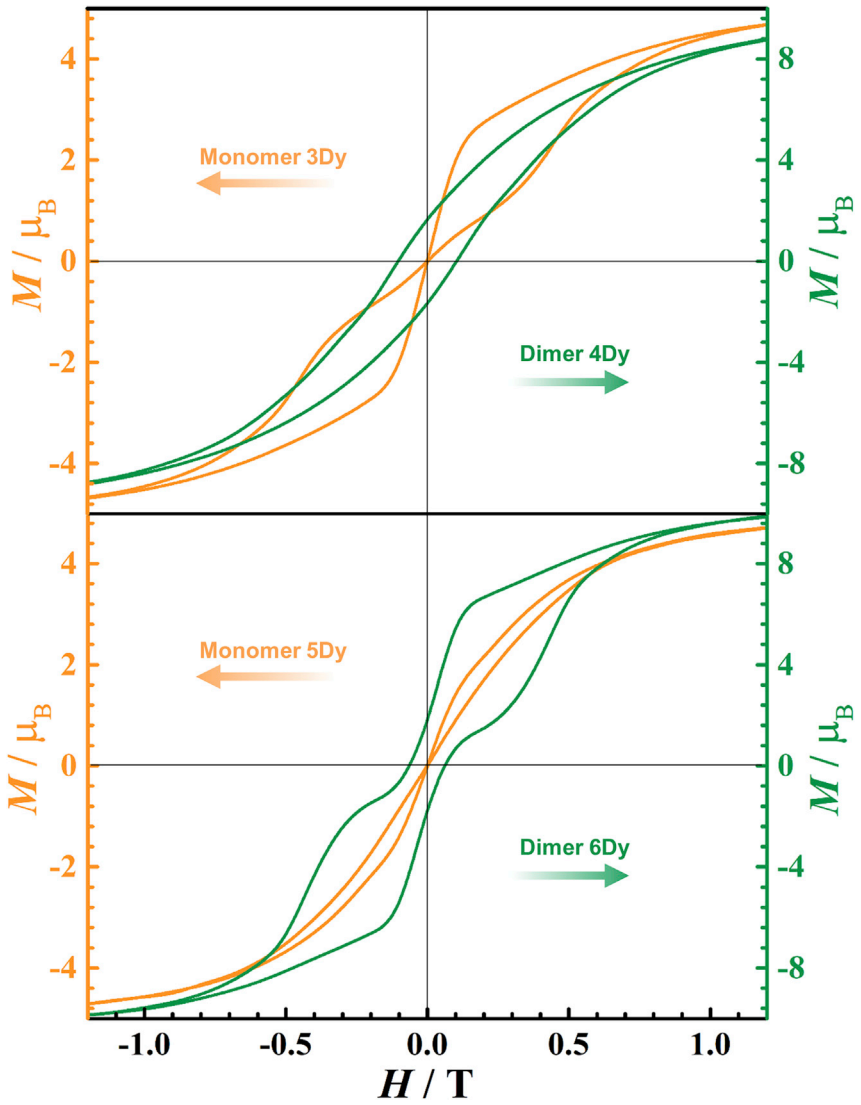

Figure 5. The magnetic hysteresis measurements

The comparison of magnetic hysteresis loops between polycrystalline samples **3Dy** and **4Dy** (top); **5Dy** and **6Dy** (bottom) at 2 K under an average sweep rate of 15 Oe s−1

antiferro (−) magnetic interactions. The strength of total exchange coupling follows a trend of descending. With regard to J_{exch}, the values of **2Dy** (−1.76 cm^{-1}) and **4Dy** (−1.83 cm^{-1}) are approaching due to the similar distance between magnetic centers of 4.08 Å and 4.16 Å, respectively, hinting this part of magnetic exchange goes through resemble path, while longer distance of 6.91 Å for **6Dy** creates less J_{exch} (−0.78 cm^{-1}). Under Ising approximation, g in Equation 2 can be replaced by g_z to calculated J_{dip} values. Despite approximate g_z values of their ground states, yet the angle between magnetic axis at both magnetic centers is different as well as the angle between magnetic axis and the connection of magnetic ions, leading to diverse dipole-dipole interactions with corresponding J_{dip} values 0.64 cm^{-1}, 1.14 cm^{-1}, and 0.37 cm^{-1} of **2Dy**, **4Dy,** and **6Dy**, respectively. **2Dy** and **4Dy** possess the same ligands, but the dipole-dipole interactions are distinctive, resulting from different *closo*- and *exo*-linkage coordination modes of C_2B_3 pentagonal facing to Dy(III). Consequently, the flexible coordination ways of carboranyl ligand can be realized by synthesis to control the magnetic exchange interaction via adjusting magnetic axis orientation. For **6Dy**, because of the farthest distance between the magnetic centers, the J_{dip} is naturally the smallest. On the whole, the larger J_{total} values for **2Dy** and **4Dy** are presumably contributed from the $B{-}H^{\delta-}\cdots Dy^{3+}$ IHBs, which is much stronger than the $B{-}H^{\delta-}\cdots Na^{+}$ in **6Dy**. Moreover, we analyzed dc

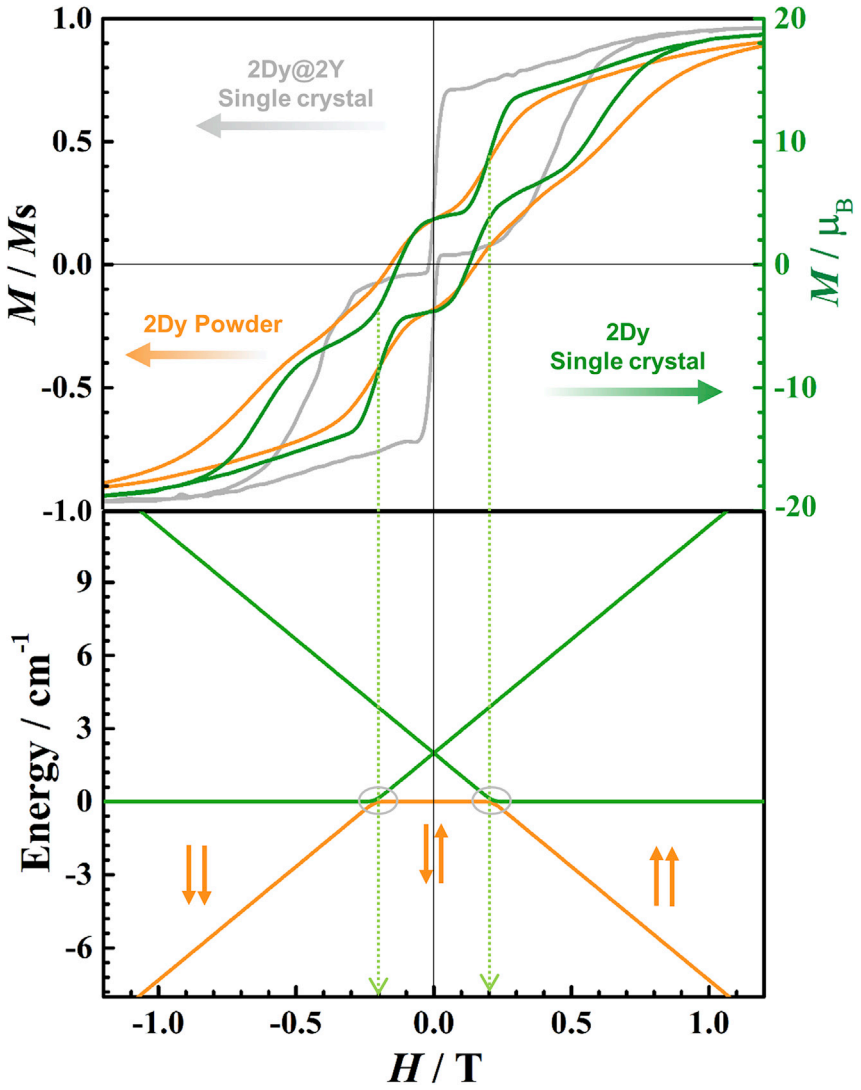

Figure 6. The magnetic hysteresis measurements and Zeeman diagram

(Top) The magnetic hysteresis loop measurements (top) at 2.0 K for single crystal sample of **2Dy** (green), **2Dy@2Y** (gray) with sweep rate 7 Oe/s and powder sample of **2Dy** (orange) with sweep rate 15 Oe/s.

(Bottom) the simulated Zeeman diagram for the single crystal sample of **2Dy**.

magnetic data of single crystal sample of **2Dy** and performed the fitting of magnetic interaction from *z* axis direction using PHI code. The coupling constant J_{zz} is coinciding with the sum of J_{zz} components of *J* matrix and the Zeeman diagram from POLY_ANISO (Figure 6, bottom), giving much reliable coupling constant of $-2.01\ cm^{-1}$, which is comparable to the coupling values $J = +4.4\ cm^{-1}$ and $J = -4.6\ cm^{-1}$ transferred from single or double oxygen anion bridged Dy(III) dimers (Wang, et al., 2021; Xiong et al., 2017) and even larger than that of double chloride bridged Dy(III) dimers with $J = -0.83\ cm^{-1}$ and $J = -1.48\ cm^{-1}$, respectively (Han, et al., 2020; Han, et al., 2019).

Table 1. Magnetic coupling constants (cm^{-1}) between two Dy(III) sites of 2Dy, 4Dy, and 6Dy

Complexes	J_{exch}	J_{dip}	J_{total}	J_{zz}
2Dy	−1.76(1)	0.64(2)	−1.12(2)	−2.01(2)
4Dy	−1.83(1)	1.14(1)	−0.69(2)	/
6Dy	−0.78(1)	0.37(2)	−0.41(2)	/

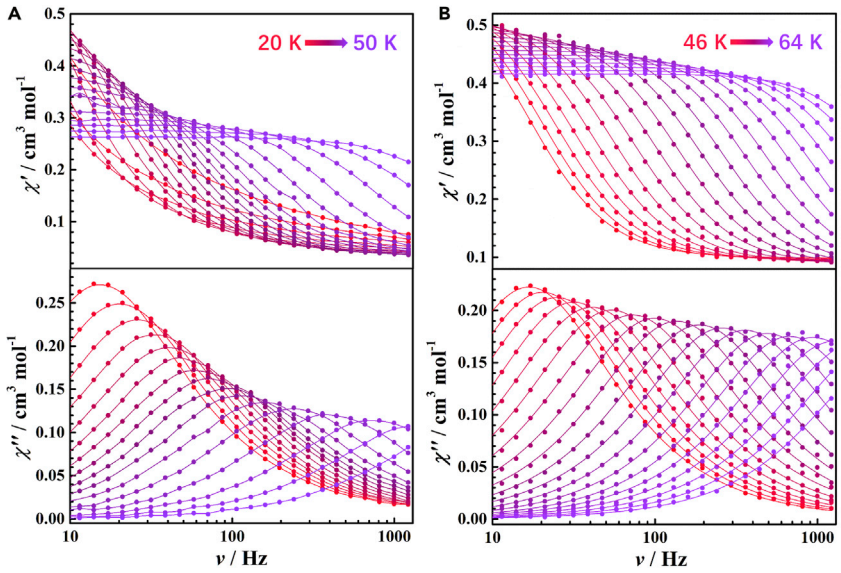

Figure 7. The AC magnetic susceptibility measurements

Frequency-dependence of the in-phase (χ′, top) and out-of-phase (χ ″, bottom) ac susceptibility signals for polycrystalline sample of **1Dy** (A) and **2Dy** (B) in zero DC field and an oscillating field of 3.5 Oe.

Dynamic magnetism

As these complexes demonstrate the SMM behavior, we analyze the dynamics of the magnetization using alternative current (ac) magnetic measurements (Figures 7 and S44–S65). The temperature- and frequency-dependent ac susceptibilities for **1Dy**, **2Dy**, **2Dy@2Y**, **3Dy**, **4Dy**, **5Dy@5Y**, **6Dy,** and **6Dy@6Y** are showed in Figures S44–S55, which can be fitted by CC-FIT program to obtain the log-log plots of τ^{-1} vs T (Figures 8, S64, and S65) (Chilton, 2014). All of the plots obey the Arrhenius law $\tau^{-1} = \tau_0^{-1} e^{-U_{eff}/T}$ in the high temperature regime and are consistent with an Orbach relaxation mechanism over an effective energy barrier U_{eff}, except for **2Dy@2Y**, which can be well fitted with $\tau^{-1} = CT^n$. The plots become power-law CT^n temperature dependence along with the fall of temperature, which is the characteristic of a two-phonon Raman process. However, in contrast with **2Dy**, **4Dy,** and **6Dy**, the magnetic relaxation process of **1Dy** and **3Dy** is accelerated below 10 K due to the zero-field QTM process. In this case, the relaxation times of dimers **2Dy**, **4Dy,**

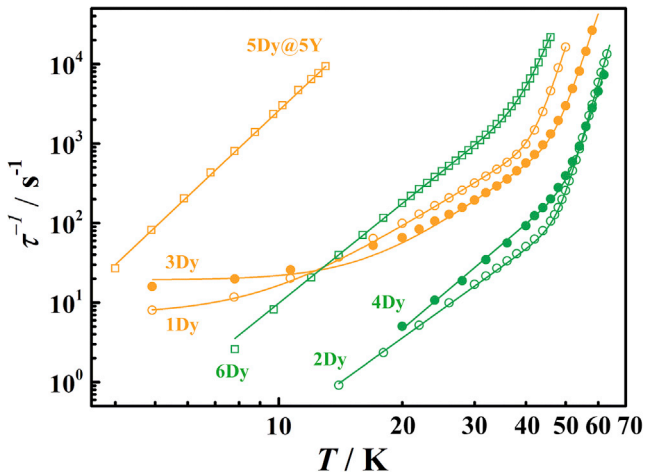

Figure 8. Plot of natural log of the inverse relaxation time vs. temperature for 1Dy, 2Dy, 3Dy, 4Dy, 5Dy@5y, and 6Dy

The plots are from the ac susceptibility measurements. The lines are best fit with Equation 4.

Table 2. The magnetic relaxation parameters of 1Dy, 2Dy, 2Dy@2Y, 3Dy, 4Dy, 5Dy@5Y, 6Dy, and 6Dy@6Y

Complexes	U_{eff} (K)	$\tau_0 \times 10^{-12}$ (s)	C (s^{-1} K^{-n})	n	τ_{QTM} (s)
1Dy	830(7)	4.2(2)	$5.9(3)\times10^{-3}$	3.2(1)	0.14(1)
2Dy	1089(6)	2.4(1)	$5.5(2)\times10^{-5}$	3.7(2)	/
2Dy@2Y	1089(6)	2.3(1)	$1.3(2)\times10^{-4}$	3.56(2)	/
3Dy	940(5)	3.9(1)	$4.5(2)\times10^{-4}$	3.78(1)	0.052(1)
4Dy	1106(5)	2.5(1)	$9.0(1)\times10^{-6}$	4.39(1)	/
5Dy@5Y	/	/	$3.5(2)10^{-2}$	4.87(2)	/
6Dy	704(10)	12.8(2)	$7.0(2)\times10^{-4}$	4.16(2)	/
6Dy@6Y	704(10)	12.5(1)	$2.0(1)\times10^{-4}$	4.5(1)	/

and **6Dy** and monomers **1Dy** and **3Dy** could be well fitted by the Equation 3. The fitting gives parameters summarized in Table 2.

$$\tau^{-1} = {\tau_0}^{-1} e^{-U_{eff}/T} + CT^n + {\tau^{-1}}_{QTM} \quad \text{(Equation 4)}$$

From Table 2 we can see all the dimeric complexes (**2Dy**, **4Dy,** and **6Dy**) possess much higher energy barriers, U_{eff} = 1089(6) K for **2Dy**, 1106(5) K for **4Dy,** and 704(10) K for **6Dy**, if compared to their corresponding monomers, U_{eff} = 830(7) K for **1Dy**, 940(5) K for **3Dy** and none for **5Dy@5Y** (Table 2). It's worth noting that the U_{eff} values of **2Dy** and **4Dy** above 1000 K are very high for polynuclear SMMs (Wang, et al., 2021; Han, et al., 2020; Krylov, et al., 2017; Gould, et al., 2020; Meng, et al., 2020). The only higher value is reported in the compound $Dy_2ScN@C_{80}$-I_h with U_{eff} = 1735 ± 21 K (Krylov, et al., 2017). Moreover, the imidazolin-iminato incorporated dysprosium complexes **1Dy**, **2Dy**, **3Dy,** and **4Dy** exhibit larger U_{eff} than phenol derivative incorporated ones **5Dy** and **6Dy** do, which is attributed to the stronger electron donating ability of $Im^{Dipp}N^-$ than that of OAr^{*-} (Trambitas, et al., 2011; Liu, et al., 2019).

CASSCF-SO calculations were performed to gain insight into the electronic structure of Dy(III) ions and understand their magnetic properties. For **1Dy** and **3Dy**, as expected, pure $|\pm15/2>$ Kramers Doublets (KDs) have been stabilized by the crystal field in the two mononuclear complexes, reflecting a strong axial coordination to the central ion site. For **1Dy**, the first and second excited KDs are fairly pure, 95.1% $|\pm13/2>$ and 78.9% $|\pm11/2>$ respectively, but the proportion of $|\pm9/2>$ in third excited KDs is only 43.5%, indicating that magnetic relaxation pathway passes between the second and third excited ones (778 K and 930 K), which is consistent with the experimental value. Naturally, those are the similar cases for **3Dy** whose calculated barriers is 906 K–1026 K. Furthermore, **3Dy** possesses higher barrier due to its purer KDs, demonstrating more fairly pure doublets benefit the increment of energy barrier in our system. For their dimer counterparts, their single ion fragments were considered to perform calculations at identical level, due to the fact that the energy barrier of binuclear compound primarily originates from single magnetic ion. These three fragments of centrosymmetric complexes **2Dy**, **4Dy,** and **6Dy** possess much higher energy barriers owing to less equatorial coordinated THF solvent, which don't make evident QTM process emerging until higher KDs. In addition, the principal magnetic axis of the ground KD of **1Dy, 2Dy, 3Dy, 4Dy, 5Dy, and 6Dy** are toward to N or O of $Im^{Dipp}N^-$ and OAr^{*-} instead of the C_2B_3 face centroid (Figures S66–S71), indicating the σ donor ligand has stronger influence on the magnetic anisotropy if compared to the π type dicarbollide ligand. Both results show their ground states agree with the Ising limit state ($g_x = g_y = 0$, g_z = 19.87 for **2Dy**; $g_x = g_y = 0$, g_z = 19.83 for **4Dy**); $g_x = g_y = 0$, g_z = 19.82 for **6Dy**) (Tables S17, S19, and S21). Moreover, all the imidazolin-iminato incorporated dysprosiacarborane dimeric complexes show larger U_{eff} compared to pure dicarbollide-based dysprosium(III) SMMs.[26] Apart from magnetic coupling constants and Zeeman diagrams, the exchange energies and g_z values corresponding to the exchange doublets were also output by POLY_ANISO and listed in Tables S28–S30, where the exchange energies for **2Dy**, **4Dy,** and **6Dy** are 1.676 cm^{-1}, 1.036 cm^{-1}, and 1.006 cm^{-1}, as well as g_z values of the first excited doublets 39.748, 39.757, and 39.650, respectively.

Conclusion

In conclusion, ten lanthanacarborane complexes were synthesized to study the unusual $B-H^{\delta-}\cdots M^{n+}$ IHBs, and found that the bonding strength is cation dependent and is determined to be 33.75 KJ/mol and 24.99 KJ/mol with the DFT calculations for **2Dy** and **4Dy** (M = Ln and n = 3), thereby can be used to switch on the exchange-

biasing effect between the magnetic centers and resulting in a zero-field opened hysteresis loops up to 7.7 K and 5.9 K with large coercive fields of H_c = 1600 Oe and H_c = 1000 Oe at 2 K for **2Dy** and **4Dy**, respectively. In contrast, $B-H^{\delta-}\cdots Na^{+}$ interaction in **6Dy** is much weaker (binding energy = 14.62 KJ/mol). Moreover, for **2Dy** the step-like hysteresis loops of single crystal measurement along the easy-axis gives a coupling constant $J_{zz} = -2.01(2)$ cm^{-1}, even larger than that of chloride bridged Dy(III) dimers. Intriguingly, the U_{eff} values of the imidazolin-iminato incorporated dysprosiacarborane complexes are much larger than those of the phenol analogs, suggesting stronger electron donating ability toward metal ions of the imidazolin-iminato ligand. Together, these results clearly demonstrate that the strength of $B-H^{\delta-}\cdots M^{3+}$ IHB is cation dependent and can be used to construct the exchange-biasing SMMs in a reversible way.

Limitations of the study

It should be noted that the step-like hysteresis loop of **2Dy** is present only at relatively lower temperatures. In addition, the magnetic measurement for single crystal sample is only suitable for **2Dy**, which can grow larger size crystals.

STAR★METHODS

Detailed methods are provided in the online version of this paper and include the following:

- KEY RESOURCES TABLE
- RESOURCE AVAILABILITY
  - Lead contact
  - Materials availability
  - Data and code availability
- METHOD DETAILS
  - Synthesis
  - Characterization
  - X-Ray crystallography
  - Magnetic measurements
  - Ab initio calculation
  - DFT calculation

SUPPLEMENTAL INFORMATION

Supplemental information can be found online at https://doi.org/10.1016/j.isci.2021.102760.

ACKNOWLEDGMENTS

This work was supported by the Natural Science Foundation of China (Nos. 21801202, 21773130 and 21971203), Shenzhen Science and Technology Program (JCYJ20180306170859634), State Key Laboratory for Mechanical Behavior of Materials (20182006), Xi'an Municipal Bureau of Science and Technology (201805056ZD7CG40), Cyrus Chung Ying Tang Foundation, and the Fundamental Research Funds for the Central Universities. We also thank the Instrument Analysis Center of Xi'an Jiaotong University for the assistance in MPMS-SQUID VSM measurement from Dr. Chang Huang.

AUTHOR CONTRIBUTIONS

P.-B.J. synthesized and characterized the compounds with the assistance of Y.-D.W. and Y.M.; Q.-C.L. and Y.-Q.Z. performed DFT, CASSCF calculations, and Hirshfeld surface analysis and independent gradient model; Y.-Z.Z. designed and supervised the work. P.-B.J., Q.-C.L., X.Z., C.K., X.-F.Z., Y.L., L.T., and Y.-Z.Z. contributed to writing the manuscript.

DECLARATION OF INTERESTS

The authors declare no competing interests.

Received: March 22, 2021
Revised: May 7, 2021
Accepted: June 18, 2021
Published: July 23, 2021

REFERENCES

Axtell, J.C., Kirlikovali, K.O., Djurovich, P.I., Jung, D., Nguyen, V.T., Munekiyo, B., Royappa, A.T., Rheingold, A.L., and Spokoyny, A.M. (2016). Blue phosphorescent zwitterionic iridium(III) complexes featuring weakly coordinating nido-carborane-based ligands. J. Am. Chem. Soc. *138*, 15758–15765.

Bader, F.W. (1994). Atoms in Molecules: A Quantum Theory (Oxford University Press).

Baker, R.T., King, R.E., Knobler, C., O'Con, C.A., and Hawthorne, M.F. (1978). Characterization and molecular structure of $[(PPh_3)RhC_2B_9H_{11}]_2$, a phosphinorhodacarborane dimer containing rhodium-hydrogen-boron bridges. J. Am. Chem. Soc. *100*, 8266–8267.

Behnken, P.E., Marder, T.B., Baker, R.T., Knobler, C.B., Thompson, M.R., and Hawthorne, M.F. (1985). Synthesis, structural characterization, and stereospecificity in the formation of bimetallic rhodacarborane Clusters Containing rhodium-hydrogen-boron bridge Interactions. J. Am. Chem. Soc. *107*, 932–940.

Blanco, F., Solimannejad, M., Alkorta, I., and Elguero, J. (2008). Inverse hydrogen bonds between XeH2 and hydride and fluoride derivatives of Li, Be, Na and Mg. Theor. Chem. Account *121*, 181–186.

Bogani, L., and Wernsdorfer, W. (2008). Molecular spintronics using single-molecule magnets. Nat. Mater. *7*, 179–186.

Braga, D., Grepioni, F., and Orpen, A.G. (1999). Crystal Engineering: From Molecules and Crystals to Materials (Springer).

Canaj, A.B., Singh, M.K., Wilson, C., Rajaraman, G., and Murrie, M. (2018). Chemical and in silico tuning of the magnetisation reversal barrier in pentagonal bipyramidal Dy(III) single-ion magnets. Chem. Commun. *54*, 8273.

Cheung, M.S., Chan, H.S., Bi, S.W., Lin, Z.Y., and Xie, Z.W. (2005). Functional sidearm promoted electron-transfer reactions: a new route to metallacarboranes incorporating the η^7-arachno-carboranyl ligands. Organometallics *24*, 4333–4336.

Chibotaru, L.F., and Ungur, L. (2006). Program POLY_ANISO (University of Leuven).

Chilton, N.F. (2014). CC-fit. http://www.nfchilton.com/cc-fit.html.

Chilton, N.F., Anderson, R.P., Turner, L.D., Soncini, A., and Murray, K.S. (2013). PHI: a powerful new program for the analysis of anisotropic monomeric and exchange-coupled polynuclear d- and f-block complexes. J. Comput. Chem. *34*, 1164–1175.

Chui, K., Yang, Q., Mak, T.C.W., Lam, W.-H., Lin, Z.-Y., and Xie, Z.-W. (2000). Synthesis, structure, and bonding of d^0/f^n metallacarboranes incorporating the η^7-carboranyl ligand. J. Am. Chem. Soc. *122*, 5758–5764.

Cui, P.-F., Lin, Y.-J., Li, Z.-H., and Jin, G.-X. (2020). Dihydrogen bond interaction induced separation of hexane isomers by self-assembled carborane metallacycles. J. Am. Chem. Soc. *142*, 8532–8538.

Cundari, T.R., and Stevens, W.J. (1993). Effective core potential methods for the lanthanides. J. Chem. Phys. *98*, 5555–5565.

Dolomanov, O.V., Bourhis, L.J., Gildea, R.J., Howard, J.A.K., and Puschmann, H. (2009). OLEX2: a complete structure solution, refinement and analysis program. J. Appl. Crystallogr. *42*, 339–341.

Frisch, M.J., Trucks, G.W., Schlegel, H.B., Scuseria, G.E., Robb, M.A., Cheeseman, J.R., Scalmani, G., Barone, V., Mennucci, B., Petersson, G.A., et al. (2009). Gaussian 09 (Gaussian, Inc.).

Gatteschi, D., Sessoli, R., and Villain, J. (2006). Molecular Nanomagnets (Oxford University Press).

Gould, C.A., Mu, E., Vieru, V., Darago, L.E., Chakarawet, K., Gonzalez, M.I., Demir, S., and Long, J.R. (2020). Substituent effects on exchange coupling and magnetic relaxation in 2,2'-bipyrimidine radical-bridged dilanthanide complexes. J. Am. Chem. Soc. *142*, 21197–21209.

Grimme, S. (2004). Accurate description of van der Waals complexes by density functional theory including empirical corrections. J. Comput. Chem. *25*, 1463–1473.

Grimme, S. (2006). Semiempirical GGA-type density functional constructed with a long-range dispersion correction. J. Comput. Chem. *27*, 1787–1799.

Grimme, S. (2011). Density functional theory with London dispersion corrections. Wiley Interdiscip. Rev. Comput. Mol. Sci. *1*, 211–228.

Gronert, S. (1993). Theoretical studies of proton transfers. 1. the potential energy surfaces of the identity reactions of the first-and second-row non-metal hydrides with their conjugate bases. J. Am. Chem. Soc. *115*, 10258–10266.

Gu, Y., Kar, T., and Scheiner, S. (1999). Fundamental properties of the CH•••O interaction: is it a true hydrogen bond? J. Am. Chem. Soc. *121*, 9411–9422.

Gupta, S.K., Rajeshkumar, T., Rajaraman, G., and Murugavel, R. (2016a). An air-stable Dy(iii) single-ion magnet with high anisotropy barrier and blocking temperature. Chem. Sci. *7*, 5181–5191.

Gupta, T., Velmurugan, G., Rajeshkumar, T., and Rajaraman, G. (2016b). Role of lanthanide-ligand bonding in the magnetization relaxation of mononuclear single-ion magnets: a case study on pyrazole and carbene ligated Ln^{III} (Ln=Tb, Dy, Ho, Er) complexes. J. Chem. Sci. *128*, 1615–1630.

Han, T., Ding, Y.-S., Li, Z.-H., Yu, K.-X., Zhai, Y.-Q., Chilton, N.F., and Zheng, Y.-Z. (2019). Dichlorido-bridged dinuclear Dy(III) single-molecule magnet with an effective energy barrier larger than 600 K. Chem. Commun. *55*, 7930–7933.

Han, T., Giansiracusa, M.J., Li, Z.-H., Ding, Y.-S., Chilton, N.F., Winpenny, R.E.P., and Zheng, Y.-Z. (2020). Exchange-biasing in a dinuclear dysprosium(III) single-molecule magnet with a large energy barrier for magnetization reversal. Chem. Eur. J. *26*, 6773–6777.

Hannon, M.J. (2007). Supramolecular DNA recognition. Chem. Soc. Rev. *36*, 280–295.

Hewes, J.D., Kreimendahl, C.W., Mardcr, T.B., and Hawthorne, M.F. (1984). Metal-promoted insertion of an activated alkene into a boron-hydrogen bond of an exopolyhedral nido-rhodacarborane: rhodium-catalyzed hydroboration. J. Am. Chem. Soc. *106*, 5757–5759.

Hosmane, N.S. (2011). Boron Science: New Technologies and Applications (Chemical Rubber Company), pp. 792–878.

Howard, J.A.K., Hoy, V.J., O'Hagan, D., and Smith, G.T. (1996). How good is fluorine as a hydrogen bond acceptor? Tetrahedron *52*, 12613–12622.

Humphrey, W., Dalke, A., and Schulten, K. (1996). VMD: visual molecular dynamics. J. Mol. Graphics. *14*, 33–38.

Ignacio, F., Galván, M., Ali, A., Celestino, A., Francesco, A., Jochen, A., Jie, J.B., Sergey, I.B., Nikolay, A.B., Rebecca, K.C., et al. (2019). OpenMolcas: from source code to insight. J. Chem. Theor. Comput. *15*, 5925–5964.

Jin, P.-B., Zhai, Y.-Q., Yu, K.-X., Winpenny, R.E.P., and Zheng, Y.-Z. (2020). Dysprosiacarboranes as organometallic single-molecule magnets. Angew. Chem. Int. Ed. *59*, 9350–9354.

Katie, L.M.H., Jennifer, J.L.R., Liviu, U., Rebecca, J.H., Ilia, K., and Muralee, M. (2017). Cycloheptatrienyl trianion: an elusive bridge in the search of exchange coupled dinuclear organolanthanide single-molecule magnets. Chem. Sci. *8*, 231–240.

Kolandaivel, P., and Nirmala, V. (2004). Study of proper and improper hydrogen bonding using bader's atoms in molecules (AIM) theory and NBO analysis. J. Mol. Struct. *694*, 33–38.

Krylov, D.S., Liu, F., Avdoshenko, S.M., Spree, L., Weise, B., Waske, A., Wolter, A.U.B., Büchner, B., and Popov, A.A. (2017). Record-high thermal barrier of the relaxation of magnetization in the nitride clusterfullerene $Dy_2ScN@C_{80}$-I_h. Chem. Commun. *53*, 7901–7904.

Kuduva, R.V., Stuart, K.L., Boujemaa, M., Keith, S.M., and Gopalan, R. (2018). Understanding the mechanism of magnetic relaxation in pentanuclear {MnIVMnIII2LnIII2} single-molecule magnets. Inorg. Chem. *57*, 1158–1170.

Kwong, W.-C., Chan, H.-S., Tang, Y., and Xie, Z.-W. (2004). Substituent effects. synthesis and structural characterization of group 4 metallacarboranes containing $(C_6H_5CH_2)_2C_2B_9H_9^{2-}$ and $[o\text{-}C_6H_4(CH_2)_2]C_2B_9H_9^{2-}$ Ligands. Organometallics *23*, 4301.

Lefebvre, C., Rubez, G., Khartabil, H., Boisson, J.-C., Contreras-García, J., and Hénon, E. (2017). Accurately extracting the signature of intermolecular interactions present in the NCI plot of the reduced density gradient versus electron density. Phys. Chem. Chem. Phys. *19*, 17928–17936.

Leuenberger, M.N., and Loss, D. (2001). Quantum computing in molecular magnets. Nature *410*, 789–793.

Liu, Q., and Hoffmann, R. (1995). Theoretical aspects of a novel mode of hydrogen-hydrogen bonding. J. Am. Chem. Soc. *117*, 10108–10112.

Liu, B.-C., Ge, N., Zhai, Y.-Q., Zhang, T., Ding, Y.-S., and Zheng, Y.-Z. (2019). Imido ligand significantly enhances the effective energy barrier of dysprosium(III) single-molecule magnets. Chem. Commun. *55*, 9355–9358.

Lu, T., and Chen, F.-W. (2012a). Multiwfn: a multifunctional wavefunction analyzer. J. Comput. Chem. *33*, 580–592.

Lu, T., and Chen, F.-W. (2012b). Quantitative analysis of molecular surface based on improved marching tetrahedra algorithm. J. Mol. Graph. Model. *38*, 314–323.

Malmqvist, P.A., Roos, B.O., and Schimmelpfennig, B. (2002). The restricted active space (RAS) state interaction approach with spin–orbit coupling. Chem. Phys. Lett. *357*, 230–240.

Mannini, M., Pineider, F., Sainctavit, P., Danieli, C., Otero, E., Sciancalepore, C., Talarico, A.M., Arrio, M.A., Cornia, A., Gatteschi, D., and Sessoli, R. (2009). Magnetic memory of a singlemolecule quantum magnet wired to a gold surface. Nat. Mater. *8*, 194–197.

Meng, Y.-S., Xiong, J., Yang, M.-W., Qiao, Y.-S., Zhong, Z.-Q., Sun, H.-L., Han, J.-B., Liu, T., Wang, B.-W., and Gao, S. (2020). Experimental determination of magnetic anisotropy in exchange-bias dysprosium metallocene single-molecule magnets. Angew. Chem. Int. Ed. *59*, 13037–13043.

Nava, A., Rigamonti, L., Zangrando, E., Sessoli, R., Wernsdorfer, W., and Cornia, A. (2015). Redox-controlled exchange bias in a supramolecular chain of Fe4 single-molecule magnets. Angew. Chem. Int. Ed. *54*, 8777–8782.

Nguyen, T.N., Wernsdorfer, W., Shiddiq, M., Abboud, K.A., Hill, S., and Christou, G. (2016). Supramolecular aggregates of single-molecule magnets: exchange-biased quantum tunneling of magnetization in a rectangular $[Mn_3]_4$ Tetramer. Chem. Sci. *7*, 1156–1173.

Norre, M.S., Gao, C., Dey, S., Gupta, S.K., Borah, A., Murugavel, R., Rajaraman, G., and Overgaard, Jacob. (2020). High-pressure crystallographic and magnetic studies of pseudo-D_{5h} symmetric Dy(III) and Ho(III) single-molecule magnets. Inorg. Chem. *59*, 717–729.

Núñez, R., Romero, I., Teixidor, F., and Viñas, C. (2016). Icosahedral boron clusters: a perfect tool for the enhancement of polymer features. Chem. Soc. Rev. *45*, 5147–5173.

Panda, T.K., Trambitas, A.G., Bannenberg, T., Hrib, C.G., Randoll, S., Jones, P.G., and Tamm, M. (2009). Imidazolin-2-iminato complexes of rare earth metals with very short metal−nitrogen bonds: experimental and theoretical studies. Inorg. Chem. *48*, 5462–5472.

Pauling, L. (1960). The Nature of the Chemical Bond, 3rd ed (Cornell University).

Perdew, J.P., Burke, K., and Ernzerhof, M. (1997). Generalized gradient approximation made simple. Phys. Rev. Lett. *78*, 1396.

Reed, J.B., Hopkins, B., Audrieth, L., Selwood, P., Ward, R., and Dejong, J. (1939). Anhydrous rare earth chlorides. Inorg. Synth. *1*, 28.

Rodham, D.A., Suzuki, S., Suenram, R.D., Lovas, F.J., Dasgupta, S., Goddard, W.A., III, and Blake, G.A. (1993). Hydrogen bonding in the benzene–ammonia dimer. Nature *362*, 735–737.

Roos, B.O., Lindh, R., Malmqvist, P.-Å., Veryazov, V., and Widmark, P.-O. (2004). Main group atoms and dimers studied with a new relativistic ANO basis Set. J. Phys. Chem. A *108*, 2851–2858.

Roos, B.O., Lindh, R., Malmqvist, P.-Å., Veryazov, V., and Widmark, P.-O. (2005). New relativistic ANO basis sets for actinide atoms. Chem. Phys. Lett. *409*, 295–299.

Rozas, I., Alkorta, I., and Elguero, J. (1997). Inverse hydrogen-bonded complexes. J. Phys. Chem. A *101*, 4236–4244.

Silva, L.C., and Hardie, M.J. (2012). Exploring Ag···H–B interactions in coordination polymers: silver–alkanedinitrile net-works with cobalt carbaborane anions. CrystEngComm *14*, 3367–3372.

Spackman, M.A., and Jayatilakaa, D. (2009). Hirshfeld surface analysis. CrystEngComm *11*, 19–32.

Steiner, T. (2002). The hydrogen bond in the solid state. Angew. Chem. Int. Ed. *41*, 48–76.

Tamm, M., Petrovic, D., Randoll, S., Beer, S., Bannenberg, T., Jones, P.G., and Grunenberg. (2007). Structural and theoretical investigation of 2-iminoimidazolines - carbene analogues of iminophosphoranes. J. Org. Biomol. Chem. *5*, 523–530.

Trambitas, A.G., Yang, J., Melcher, D., Daniliuc, C.G., Jones, P.G., Xie, Z.-W., and Tamm, M. (2011). Synthesis and structure of rare-earth-metal dicarbollide complexes with an imidazolin-2-iminato ligand featuring very short metal-nitrogen bonds. Organometallics *30*, 1122–1129.

Wang, J., Li, S., Zheng, C., Maguire, J.A., Sarkar, B., Kaim, W., and Hosmane, N.S. (2003). Chemistry of C-trimethylsilyl-substituted heterocarboranes. 29. synthetic and structural studies on lanthanacarboranes with two and three "carbons apart" carborane cages bonding to Ln(III) metal (Ln(III) = Nd, Gd, Dy, Ho, Er, Tb, Lu). Organometallics *22*, 4334–4342.

Wang, J., Li, Q.-W., Wu, S.-G., Chen, Y.-C., Wan, R.-C., Huang, G.-Z., Liu, Y., Liu, J.-L., Reta, D., Giansiracusa, M.J., et al. (2021). Opening magnetic hysteresis by axial ferromagnetic coupling: from mono-decker to double-decker metallacrown. Angew. Chem. Int. Ed. *60*, 5299–5306.

Wernsdorfer, W., Aliaga-Alcalde, N., Hendrickson, D.N., and Christou, G. (2002). Exchange-biased quantum tunnelling in a supramolecular dimer of single-molecule magnets. Nature *416*, 406–409.

Xie, Z.-W., Liu, Z.-X., Chiu, K.-Y., Xue, F., and Mak, T.C.W. (1997). Synthesis and structural characterization of closo- and exo-nido-lanthanacarboranes. Organometallics *16*, 2460.

Xie, Z.W., Liu, Z.X., Yang, Q.C., and Mak, T.C.W. (1999). exo-nido- versus closo-lanthanacarboranes. synthesis and structure of exo-nido-$[(C_6H_5CH_2)_2C_2B_{10}H_{10}]Ln(DME)_3$, $[exo\text{-}nido\text{-}\{(C_6H_5CH_2)_2C_2B_9H_9\}Ln(THF)_3]_2$ (Ln = Sm, Yb), and closo-exo-$[(C_6H_5CH_2)_2C_2B_{10}H_{10}]_4Sm_2Na_3$. Organometallics *18*, 3603–3609.

Xing, H., Zhang, Y., Hu, J., Krishna, R., Wang, L., Yang, L., Cui, X., and Duttwyler, S. (2020). Rational design of microporous MOFs with anionic boron cluster functionality and cooperative dihydrogen binding sites for highly selective capture of acetylene. Angew. Chem. Int. Ed. *59*, 17664–17669.

Xiong, J., Ding, H.-Y., Meng, Y.-S., Gao, C., Zhang, X.-J., Meng, Z.-S., Zhang, Y.-Q., Shi, W., Wang, B.-W., and Gao, S. (2017). Hydroxide-bridged five-coordinate DyIII single-molecule magnet exhibiting the record thermal relaxation barrier of magnetization among lanthanide-only dimers. Chem. Sci. *8*, 1288–1294.

Yu, K.-X., Kragskow, J.G.C., Ding, Y.-S., Zhai, Y.-Q., Reta, D., and Chilton, N.F. (2020). Enhancing magnetic hysteresis in single-molecule magnets by ligand functionalization. Chem *6*, 1777–1793.

Yuan, K., Zuo, G.-F., Liu, Y.-Z., Zhu, Y.-C., Liu, X.-W., and Zhang, J.-Y. (2011). Inverse hydrogen bonds between SiH4 and hydrides of Na, Mg and Be. Sci. China Chem. *54*, 186–193.

Zhang, X.-L., Dai, H.-M., Yan, H., Zou, W.-L., and Cremer, D. (2016). B–H···π interaction: a new type of nonclassical hydrogen bonding. J. Am. Chem. Soc. *138*, 4334–4337.

Zhang, H.-L., Zhai, Y.-Q., Qin, L., Ungur, L., Nojiri, H., and Zheng, Y.-Z. (2020). Single-molecule toroic design through magnetic exchange coupling. Matter *2*, 1481–1493.

Zhao, D., and Xie, Z. (2016). Recent advances in the chemistry of carborynes. Coord. Chem. Rev. *314*, 14–33.

STAR★METHODS

KEY RESOURCES TABLE

REAGENT or RESOURCE	SOURCE	IDENTIFIER
Deposited data		
Crystal data for **1Dy**	[CCDC]: [2047062]	Deposition Number: 2047062
Crystal data for **2Dy**	[CCDC]: [2047063]	2047063
Crystal data for **2Y**	[CCDC]: [2047064]	2047064
Crystal data for **3Dy**	[CCDC]: [2047065]	2047065
Crystal data for **4Dy**	[CCDC]: [2047066]	2047066
Crystal data for **5Dy**	[CCDC]: [2058168]	2058168
Crystal data for **5Y**	[CCDC]: [2058169]	2058169
Crystal data for **6Dy**	[CCDC]: [2058167]	2058167
Crystal data for **6Y**	[CCDC]: [2058170]	2058170
Software and algorithms		
OPEN MOLCAS	Ignacio, et al., 2019	http://www.molcas.org/
Gaussian	Frisch, et al., 2009	http://gaussian.com/
Multiwfn	Lu and Chen (2012a), 2012b	http://sobereva.com/multiwfn/
VMD	Humphrey, et al., 1996	https://www.ks.uiuc.edu/Research/vmd/
COCO-FIT	Chilton (2014)	http://www.nfchilton.com/cc-fit.html.
PHI	Chilton, et al., 2013	http://www.nfchilton.com/phi.html

RESOURCE AVAILABILITY

Lead contact

Further information and requests for resources should be directed to and will be fulfilled by the lead contact, Yan-Zhen Zheng (zheng.yanzhen@xjtu.edu.cn).

Materials availability

All materials generated in this study are available from the lead contact without restriction.

Data and code availability

Crystal data for (**1Dy**), (**2Dy**), (**2Y**), (**3Dy**), (**4Dy**), (**5Dy**), (**5Y**), (**6Dy**) and (**6Y**) are available from the Cambridge Crystallographic Data Centre under CCDC: 2047062, 2047063, 2047064, 2047065, 2047066, 2058168, 2058169, 2058167, 2058170. Computational output is available on request.

METHOD DETAILS

Synthesis

All experiments were performed under an atmosphere of dry argon with the rigid exclusion of air and moisture using standard Schlenk or in a glovebox. THF were dried and degassed by standard techniques. Anhydrous $LnCl_3$ (Ln = Dy) were prepared according to literature procedures (Reed, et al., 1939). $[Me_3NH][C_2B_9H_9]$ (Xie, et al., 1997), $[Me_3NH][o\text{-}C_6H_4(CH_2)_2\text{-}C_2B_9H_9]$ (Kwong, et al., 2004), $Im^{Dipp}NH$ (Tamm, et al., 2007), ($Im^{Dipp}NH$ represents 1,3-bis(2,6-diisopropylphenyl)imidazolin-2-imine), HOAr* (Liu, et al., 2019), (Ar* represents 2,6-bis(diphenylmethyl)-4-methylphenyl), $[(Im^{Dipp}N)MCl_2(THF)_3]$ (M = Dy, Y) (Panda, et al., 2009) and $[(OAr^*)MCl_2(THF)_3]$ (M = Dy, Y) (Liu, et al., 2019) were prepared according to the literature methods.

Synthesis of $[(Im^{Dipp}N)DyCl_2(THF)_3]$: A mixture of anhydrous $DyCl_3$ (810 mg, 3 mmol) and $LiCH_2SiMe_3$(5.4 mL, 3 mmol) (0.56M) was stirred with THF (30 mL) for 2 h. Then a solution of $Im^{Dipp}NH$ (1212 mg, 3 mmol) in THF (10 mL) was added. The reaction mixture was allowed to stir for another 12 h.

The solvent was evaporated, and the compound was repeatedly extracted with pentane (3x30 mL). The pentane was removed completely under vacuum to give pale yellow microcrystalline.

Synthesis of [($Im^{Dipp}N$)$YCl_2(THF)_3$]: Following the procedure described for [($Im^{Dipp}N$)$DyCl_2(THF)_3$]. The reaction of the solution of anhydrous YCl_3 (594 mg, 3 mmol), $LiCH_2SiMe_3$ (5.4 mL, 3 mmol) (0.56M) and $Im^{Dipp}NH$ (1212 mg, 3 mmol) in THF(40 mL) gave [($Im^{Dipp}N$)$YCl_2(THF)_3$] as white microcrystalline.

Synthesis of [(OAr*)$DyCl_2(THF)_3$]:To a suspension of NaH (60 mg, 1.5 mmol, 60 *w*% dispersed in mineral oil) in 5 mL THF was added with 5 mL THF solution of HOAr* (441 mg, 1 mmol). The mixture was allowed to stirred for 2 hours at room temperature. The $DyCl_3$ (270 mg, 1.0 mmol) was added to suspension and stirred at room temperature overnight. The suspension was allowed to settle overnight. The white precipitate was filtered off and the solvent of the filtrate was removed completely under vacuum to produce [(OAr*)$DyCl_2(THF)_3$] as pale yellow solid.

Synthesis of [(OAr*)$YCl_2(THF)_3$]: Following the procedure described for [(OAr*)$DyCl_2(THF)_3$]. The reaction of the solution of NaOAr* in THF with YCl_3 gave [(OAr*)$Cl_2(THF)_3$] as white solid.

Synthesis of [($Im^{Dipp}N$)$Dy(C_2B_9H_{11})(THF)_2$] (**1Dy**): To a suspension of NaH (80 mg, 2 mmol, 60 *w*% dispersed in mineral oil) in 10 mL THF was added with 5 mL THF solution of [Me_3NH][$C_2B_9H_{11}$] (97 mg, 0.5 mmol). The mixture was allowed to refluxed overnight. The generated Me_3N was then removed to approximately half of the solvent under vacuum. The suspension was allowed to settle overnight. The resulting upper clear solution was regarded as [Na_2][$C_2B_9H_{11}$] and then was added dropwise through a cannula to a stirred suspension of [($Im^{Dipp}N$)$Dy(THF)_3Cl_2$] (425 mg, 0.5mmol) in 20 mL THF. The reaction mixture was stirred at room temperature for 48 h and then allowed to settle. The white precipitate was filtered off and the solvent of the filtrate was removed completely under vacuum. The residue was dissolved in 5 mL THF, and X-Ray quality crystals of **1Dy** were formed by diffusion with hexane after several days. Yield 175 mg, 41.6%. Elemental analysis found (calcd.)% for $C_{37}H_{63}B_9DyN_3O_2$: C 51.92 (52.75); N 4.85 (4.98); H 8.06 (7.48). IR spectra (cm^{-1}): 3601w, 3524w, 3469w, 3391w, 3334w, 3176w, 3136w, 3105w, 3078w, 2964m, 2890m, 2504s, 2082w, 2002w, 1953m, 1885w, 1824w, 1799w, 1648w, 1611w, 1559w, 1457m,1364w, 1260w, 1186m, 1044s, 967m, 887s, 810m, 770w, 671m.

Synthesis of [($Im^{Dipp}N$)$Y(C_2B_9H_{11})(THF)_2$] (**1Y**): According to the literature methods (Trambitas, et al., 2011), The reaction of the solution of [Na_2][$C_2B_9H_{11}$] (0.5 mmol) in THF with [($Im^{Dipp}N$)$YCl_2(THF)_3$] (388 mg, 0.5 mmol) at room temperature gave **1Y** as colorless crystals after several days. Yield 330 mg, 43.0%. ^{1}H NMR (THF-d_8, 400 MHz, 25°C): δ 7.32 (m, 6H, *m*-H, *p*-H), 6.81 (s, 2H, NCH), 3.60 (d, 8H, OCH_2-THF), 2.82 (m, 4H, $CHMe_2$), 1.76 (d, 8H, CH_2CH_2-THF), 1.58 (s, 2H, BCH), 1.39-1.13 (m, 24H, $CHCH_3$) ppm; the BH signals are very broad from -2.6 to -3.5 ppm. ^{11}B NMR (THF-d_8, 400 MHz, 25°C): δ -38.3 (1B), -33.5 (1B), -22.7 (2B), -17.9 (2B), -17.1 (1B), -11.2 (2B) ppm. Elemental analysis found (calcd.)% for $C_{37}H_{63}B_9YN_3O_2$: C 57.74 (57.23); N 5.46 (5.15); H 8.19 (8.44). IR spectra (cm^{-1}): 3600m, 3338m, 3176w, 3141w, 3101w, 2968s, 2924m, 2874m, 2508s, 1974w, 1895w, 1825w, 1652m, 1612s, 1464s, 1365m, 1296w, 1252w, 1202m, 1049s, 855m, 811m, 762m, 678m.

Synthesis of [($Im^{Dipp}N$)(η^5-$C_2B_9H_{11}$)Dy(μ-H_2-$C_2B_9H_9$)(THF)]$_2$ (**2Dy**): The complex **1Dy** (420 mg, 0.5 mmol) was dissolved in toluene, filtrated and then was treated with hexane. The X-Ray quality crystals of **2Dy** were formed after several days. Yield 244 mg, 63.4%. Elemental analysis found (calcd.)% for $C_{66}H_{110}B_{18}Dy_2N_6O_2$: C 50.95 (51.45); N 5.03 (5.46); H 6.88 (7.14). IR spectra (cm^{-1}): 3623m, 3466w, 3391w, 3330w, 3277w, 3173w, 3149w, 2988w, 2980w, 2503s, 2122s, 1953m, 1879m, 1814m, 1596w,1457w, 1361w, 1256w, 1213w, 1176w, 1112w, 1034m, 967m, 905m, 847m, 810m, 761m, 674w.

The alternative method for **1Dy**: The complex **2Dy** (154 mg, 0.1 mmol) was dissolved in THF and then was treated with hexane. The X-Ray quality crystals of **1Dy** were formed after several days.

Synthesis of [($Im^{Dipp}N$)(η^5-$C_2B_9H_{11}$)Y(μ-H_2-$C_2B_9H_9$)(THF)]$_2$ (**2Y**): The complex **1Y** (384mg, 0.5 mmol) was dissolved in toluene and then was treated with hexane. The X-Ray quality crystals of **2Y** were formed after several days. Yield 227 mg, 65.3%. ^{1}H NMR (Benzene-d_6, 400 MHz, 25°C): δ 7.15 (m, 12H, *m*-H, *p*-H), 7.01, 7.69 (d, 4H, NCH), 3.55 (m, 8H, OCH_2-THF), 2.36, 2.23 (m, 8H, $CHMe_2$), 1.41 (m, 8H, CH_2CH_2-THF), 1.37, 1.35 (d, 4H, BCH), 1.13, 0.99 (d, 48H, $CHCH_3$) ppm; the BH signals are very broad from -1.8 to -2.5

ppm. ^{11}B NMR (Benzene-d_6, 400 MHz, 25°C): δ -37.2 (2B), -32.6 (2B), -21.1 (4B), -16.3 (6B), -10.2 (4B) ppm. Elemental analysis found (calcd.)% for 1391.99 $C_{66}H_{110}B_{18}N_6O_2Y_2$: C 56.13 (56.89); N 5.72 (6.03); H 8.23 (7.90). IR spectra (cm^{-1}): 3621s, 3463w, 3309w, 3131w, 3076w, 3027w, 2958s, 2928m, 2868m, 2508s, 2088m, 1953w, 1874w, 1805w, 1647m, 1593m ,1543m ,1464m, 1370m, 1212m, 1029m, 930w, 861m, 801m, 747m, 683m.

Synthesis of [(Im^{Dipp}N)Dy(η^5-*o*-xylylene-$C_2B_9H_9$)$(THF)_2$] (**3Dy**): To a suspension of NaH (80 mg, 2 mmol, 60 *w* % dispersed in mineral oil) in 10 mL THF was added with 5 mL THF solution of [Me_3NH][*o*-$C_6H_4(CH_2)_2$-$C_2B_9H_9$] (148 mg, 0.5 mmol). The mixture was allowed to refluxed overnight. The generated Me_3N was then removed to approximately half of the solvent under vacuum. The suspension was allowed to settle overnight. The resulting upper clear solution was regarded as [Na_2][*o*-$C_6H_4(CH_2)_2$-$C_2B_9H_9$] and then was added dropwise through a cannula to a stirred suspension of [(Im^{Dipp}N)$DyCl_2(THF)_3$] (425 mg, 0.5 mmol) in 20 mL THF. The reaction mixture was stirred at room temperature for 48 h and then allowed to settle. The white precipitate was filtered off and the solvent of the filtrate was removed completely under vacuum. The residue was dissolved in 5 mL THF, and X-Ray quality crystals of **3Dy** were formed by diffusion with hexane after several days. Yield 219 mg, 46.5%. Elemental analysis found (calcd.)% for $C_{45}H_{69}B_9DyN_3O_2$: C 56.88 (57.21); N 4.06 (4.45); H 7.68 (7.31). IR spectra (cm^{-1}): 3624m, 3464w, 3392w, 3327w, 3176w, 3137w, 3068w, 3023w, 2970m, 2931m, 2878m, 2832m, 2518s, 2105w, 1960w, 1887w, 1811w, 1651w, 1605m, 1468m, 1392w, 1367w, 1330w, 1258m, 1218m, 1108w, 1042s, 941m, 868w, 807m, 754m, 682m.

Synthesis of [(Im^{Dipp}N)(μ-H_4-*o*-xylylene-$C_2B_9H_5$)Dy$(THF)]_2$ (**4Dy**): The complex **3Dy** (472mg, 0.5 mmol) was dissolved in toluene and then was treated with hexane. The X-Ray quality crystals of **4Dy** were formed after several days. Yield 258 mg, 59.2%. Elemental analysis found (calcd.)% for $C_{82}H_{122}B_{18}Dy_2N_6O_2$: C 56.12 (56.44); N 4.56 (4.82); H 6.77 (7.00). IR spectra (cm^{-1}): 3609w, 3468w, 3327w, 3172w, 3141w, 2963w, 2928w, 2871w, 2522s, 2115s, 1945w, 1887w, 1811w, 1648m, 1605w, 1569w, 1532w, 1461m, 1363w,1330w, 1258w, 1212w, 1180w, 1042m, 937w, 858m, 807m, 750w, 698w.

The alternative method for **3Dy**: The complex **4Dy** (174 mg, 0.1 mmol) was dissolved in THF and then was treated with hexane. The X-Ray quality crystals of **3Dy** were formed after several days.

Synthesis of [(OAr*)$Dy(THF)_2$(η^3-Et_2-$C_2B_9H_9$)Cl][(μ-H)$_3$Na$(THF)_3$] (**5Dy**): To a suspension of NaH (160 mg, 4 mmol, 60 *w*% dispersed in mineral oil) in 5 mL THF was added with 5 mL THF solution of [Me_3NH][*o*-Et_2-$C_2B_9H_9$] (250 mg, 1 mmol). The mixture was allowed to refluxed overnight. The generated Me_3N was then removed to approximately half of the solvent under vacuum. The suspension was allowed to settle overnight. The resulting upper clear solution was regarded as [Na_2][*o*-Et_2-$C_2B_9H_9$] and then was added dropwise through a cannula to a stirred suspension of [(OAr*)$DyCl_2(THF)_3$] (890 mg, 1mmol) in 20 mL THF. The reaction mixture was stirred at room temperature for 24 h and then allowed to settle. The white precipitate was filtered off and the solvent of the filtrate was removed completely under vacuum. The residue was dissolved in 5 mL Toluene, and X-Ray quality crystals of **5Dy** were formed by diffusion with hexane after several days. Yield 533 mg, 44.1%. IR spectra (cm^{-1}): 3086w, 3061w, 3022w, 2972m, 2927m, 2868m, 2520s, 1944w, 1891w, 1814w, 1602m, 1493s, 1448s, 1370s, 1319w, 1300s, 1216w, 1173w, 1139w, 1044s, 915m, 850s, 760m, 696s.

Synthesis of [(OAr*)$Y(THF)_2$(η^3-Et_2-$C_2B_9H_9$)Cl][(μ-H)$_3$Na$(THF)_3$] (**5Y**): Following the procedure described for **5Dy**. The reaction of the solution of [Na_2][*o*-Et_2-$C_2B_9H_9$] (1 mmol) in THF with [(OAr*)$YCl_2(THF)_3$] (818 mg, 1mmol) at room temperature gave **5Y** as colorless crystals after several days. Yield 445 mg, 39.2%. ^{1}H NMR (Pyridine-d_5, 400 MHz, 25°C): δ 7.17-6.83 (m, 22H, Ar-*H*), 3.67-3.58 (m, 20H, THF), 2.85-2.76 (m, 2H, *o*-CH_2CH_3), 2.47-2.38 (m, 2H, *o*-CH_2CH_3), 2.20 (s, 2H, $CH(Ph)_2$), 1.97 (s, 3H, Me), 1.63-1.54 (m, 20H, THF), 1.34-1.30 (t, 3H, *o*-CH_2CH_3) 1.04-1.00 (t, 3H, *o*-CH_2CH_3) ppm; the BH signals are very broad from -1.3 to -2.0 ppm. ^{11}B NMR (Pyridine-d_5, 400 MHz, 25°C): δ -36.09 (1B), -34.81 (1B), -33.39 (1B), -18.03 (1B), -17.21 (1B), -13.66 (1B), -11.20 (1B), -9.77 (1B), -8.33 (1B) ppm. IR spectra (cm^{-1}): 3536s, 3086w, 3060w, 3028w, 2971m, 2926m, 2869m, 2514s, 1944w, 1885w, 1815w, 1758w, 1595m, 1493s, 1444s, 1373w, 1294m, 1184m, 1139w, 1030s, 908m, 862m, 748m, 696s.

Synthesis of [(OAr*)Dy(THF)(η^5-Et_2-$C_2B_9H_6$)Cl(μ-H)$_3$Na$(THF)_2]_2$ (**6Dy**): To a suspension of NaH (160 mg, 4 mmol, 60 *w*% dispersed in mineral oil) in 5 mL THF was added with 5 mL THF solution of [Me_3NH][*o*-Et_2-$C_2B_9H_9$] (250 mg, 1 mmol). The mixture was allowed to refluxed overnight. The generated Me_3N was

then removed to approximately half of the solvent under vacuum. The suspension was allowed to settle overnight. The resulting upper clear solution was regarded as [Na_2][*o*-Et_2-$C_2B_9H_9$] and then was added dropwise through a cannula to a stirred suspension of [(OAr*)$DyCl_2(THF)_3$] (890 mg, 1mmol) in 20 mL THF. The reaction mixture was refluxing for 48 h and then allowed to settle. The white precipitate was filtered off and the solvent of the filtrate was removed completely under vacuum. The residue was dissolved in 5 mL Toluene, and X-Ray quality crystals of **6Dy** were formed by diffusion with hexane after several days. Yield 707 mg, 33.2%. IR spectra (cm^{-1}): 3523s, 3081w, 3060w, 3024w, 2965m, 2925m, 2870m, 2514s, 1944w, 1886w, 1802w, 1756w, 1602m, 1492s, 1444s, 1370m, 1300m, 1173m, 1076w, 1032s, 915w, 858m, 747m, 696s.

The alternative method for **6Dy**: **5Dy** (302 mg, 0.25mmol) was dissolved in 20mL THF. The mixture was refluxing for 24 h and then the solvent was removed completely under vacuum. The residue was dissolved in 5 mL Toluene, and X-Ray quality crystals of **6Dy** were formed by diffusion with hexane after several days.

Synthesis of [(OAr*)Y(THF)(η^5-Et_2-$C_2B_9H_6$)Cl(μ-H)$_3$Na$(THF)_2]_2$ (**6Y**): Following the procedure described for **6Dy**. The reaction of the solution of [Na_2][*o*-Et_2-$C_2B_9H_9$] (1 mmol) in THF with [(OAr*)$YCl_2(THF)_3$] (818 mg, 1mmol) gave **6Y** as colorless crystals after several days. Yield 591 mg, 29.8%. ^{1}H NMR (Pyridine-d_5, 400 MHz, 25°C): δ 7.71-6.83 (m, 44H, Ar-*H*), 3.64-3.61 (m, 24H, THF), 2.85-2.76 (m, 4H, *o*-CH_2CH_3), 2.47-2.38 (m, 4H, *o*-CH_2CH_3), 2.20 (s, 4H, $CH(Ph)_2$), 1.97 (s, 6H, Me), 1.62-1.55 (m, 24H, THF), 1.34-1.30 (t, 6H, *o*-CH_2CH_3) 1.04-1.00 (t, 6H, *o*-CH_2CH_3) ppm; the BH signals are very broad from -1.3 to -2.0 ppm. ^{11}B NMR (Pyridine-d_5, 400 MHz, 25°C): δ -36.15 (3B), -33.41 (3B), -18.02 (4B), -17.16 (2B), -11.27 (2B), -9.76 (4B) ppm. IR spectra (cm^{-1}): 3086w, 3060w, 3028w, 2977m, 2932m, 2874m, 2508s, 1944w, 1878w, 1803w, 1595m, 1492s, 1456s, 1371w, 1300s, 1216w, 1178w, 1139w, 1042s, 915m, 844s, 761s, 696s.

The alternative method for **6Y**: **5Y** (495 mg, 0.25mmol) was dissolved in 20mL THF. The mixture was refluxing for 24 h and then the solvent was removed completely under vacuum. The residue was dissolved in 5 mL Toluene, and X-Ray quality crystals of **6Y** were formed by diffusion with hexane after several days.

Synthesis of 5% diluted sample **2Dy@2Y**: Following the procedure described for **2Dy**. The reaction of the solution of [Na_2][$C_2B_9H_9$] (1 mmol) in THF with [($Im^{Dipp}N$)$YCl_2(THF)_3$] (737 mg, 0.95mmol) and [($Im^{Dipp}N$)$DyCl_2(THF)_3$] (42.5 mg, 0.05mmol) at room temperature to give **1Dy@1Y**, which was recrystallized in toluene to form **2Dy@2Y**. The dilution ratio of dysprosium in **2Dy@2Y** was determined by ICP-MS to be 7.7% ± 0.5%. 7.7%.

Synthesis of 5% diluted sample **5Dy@5Y**: Following the procedure described for **5Dy**. The reaction of the solution of [Na_2][*o*-Et_2-$C_2B_9H_9$] (1 mmol) in THF with [(OAr*)$YCl_2(THF)_3$] (777 mg, 0.95mmol) and [(OAr*)$DyCl_2(THF)_3$] (44.5 mg, 0.05mmol) at room temperature gave **5Dy@5Y** as colorless crystals after several days. The dilution ratio of dysprosium in **5Dy@5Y** was determined by ICP-MS to be 4.1% ± 0.5%.

Synthesis of 5% diluted sample **6Dy@6Y**: Following the procedure described for **6Dy@6Y**. The reaction of the solution of [Na_2][*o*-Et_2-$C_2B_9H_9$] (1 mmol) in THF with [(OAr*)$YCl_2(THF)_3$] (777 mg, 0.95mmol) and [(OAr*)$DyCl_2(THF)_3$] (44.5 mg, 0.05mmol) at 85 oC gave **6Dy@6Y** as colorless crystals after several days. The dilution ratio of dysprosium in **6Dy@6Y** was determined by ICP-MS to be 10.6% ± 0.5%.

Characterization

NMR spectra were measured on a Bruker Avance-400 spectrometer and chemical shifts (δ) are reported in parts per million (ppm). ^{1}H NMR and ^{11}B NMR spectra were recorded at 400 MHz in NMR solvents and referenced internally to corresponding solvent resonance. Infrared spectra were collected on a Thermo Fisher Nicolet 6700 FT-IR spectrometer using ATR (Attenuated Total Reflectance) method. Absorption maxima (ν max) are reported in wavenumbers (cm^{-1}). Dilution ratios were determined with inductively coupled plasma mass spectrometry (ICP-MS; NexION350D).

X-Ray crystallography

All data were recorded on a Bruker SMART CCD diffractometer with MoKα radiation (λ = 0.71073 Å). The structures were solved by direct methods and refined on F^2 using Olex2 (Dolomanov, et al., 2009). CCDC 2047062 (**1Dy**), 2047063 (**2Dy**), 2047064 (**2Y**), 2047065 (**3Dy**), 2047066 (**4Dy**), 2058168 (**5Dy**), 2058169 (**5Y**), 2058167 (**6Dy**) and 2058170 (**6Y**) contain the supplementary crystallographic data for this paper. These data can be obtained free of charge via www.ccdc.cam.ac.uk/conts/retrieving.html (or from the Cambridge

Crystallographic Data Centre, 12 Union Road, Cambridge CB21EZ, UK; fax: (+44)1223-336-033; or deposit@ccdc.cam.ac.uk).

Magnetic measurements

Magnetic susceptibility measurements have been carried out with a Quantum Design MPMS-XL7 SQUID magnetometer upon cooling from 300 to 0.5 K in variable applied fields. Ac susceptibility measurements have been performed at frequencies of between 1 and 1218 Hz with an oscillating field of 3.5 Oe and with variable dc applied field. polycrystalline samples were embedded in eicosane to avoid any field induced crystal reorientation. A diamagnetic correction has been calculated from Pascal constants and embedding eicosane has been applied to the observed magnetic susceptibility. The magnetic hysteresis loops of 0.02 T/s and 0.05 T/s have been carried out with a Quantum Design MPMS-SQUID VSM-094 of Instrument Analysis Center of Xi'an Jiaotong University. The magnetic measurements for easy axis of single crystals were carried out with a sealed NMR tube in which the single crystal of 1.3-1.5 mg was immersed in crystal oil. The tube was then applied with 5 Tesla magnetic field for 10 min till the magnetic easy axis of single crystal along with the direction of magnetic field at 300 K. The 5 T magnetic field wasn't removed until the temperature of sample space dropped to 150 K and settled for 30 min to freeze crystal oil in tube.

Ab initio calculation

We performed CASSCF-SO (completely active space self-consistent filed spin orbit) calculation though OPEN MOLCAS (Ignacio, et al., 2019) in order to gain insight into the electronic structure of Dy(III) ions and understand the observed exchange biasing effect. The geometry of these molecules was gained from X-ray crystal structure without optimization. The basic sets from MOLCAS ANO-RCC library (Roos, et al., 2004) were employed in whole calculation tasks: VTZP quality for paramagnetic ion, VDZP quality for all atoms at the first coordination sphere and VDZ quality for the rest atoms. The active space was composed of CAS (9,7),namely seven active f-orbitals and nine active f-electrons. The states of 21 sextets, 224 quartets and 490 doublets have been computed in the RASSCF module. The spin-orbit (SO) states were obtained in the RASSI module (Malmqvist, et al., 2002) by choosing 21 sextets, 128 quartets and 130 doublets, respectively. The magnetic properties for individual Dy(III) ions were obtained through SINGLE_ANISO module (Roos, et al., 2005) like g-tensors, crystal field parameters, transition magnetic moment matrix, magnetic susceptibility as well as magnetization plot. Here for calculating dimer complexes, one of two Dy(III) sites were replaced by diamagnetic ion Lu(III) treated as the same quality in basis set aspect. Considering saving the disk space and assuring calculation accuracy, we employed the Cholesky decomposition for two-election integrals in whole calculations. To further understand the interaction between two Dy(III) centers in two centrosymmetric complexes, magnetic exchange and dipole-dipole exchange were simulated though POLY_ANISO program based on the previous results of single-ion property. POLY_ANISO program has been performed to fit dinuclear even polynuclear complexes successfully and broadly (Chibotaru and Ungur, 2006; Katie, et al., 2017; Xiong et al., 2017; Zhang, et al., 2020; Kuduva, et al., 2018). Meanwhile, we also acquired the simulated magnetization and magnetic susceptibility plots and the total coupling parameter using PHI code in order to improve the credibility of the fitting process and found that both *J* values output from distinct codes are consistent (Chilton, et al., 2013). Considering the magnetic curves output by POLY_ANISO are scatter plots and to distinguish the simulated and experimental data better, we ultimately employed the continuous simulated curves generated by PHI code (Figures S23–S27).

DFT calculation

Population analysis calculations were performed using Gaussian 09D (Frisch, et al., 2009) to acquire electrostatic potentials (ESP) and specific interaction strength for $B-H^{\delta-}\cdots Dy^{3+}$ and $B-H^{\delta-}\cdots Na^{+}$. For interaction strength calculation, the geometry of these complexes was obtained from X-ray crystal structure without optimization. To avoid convergence problems, model complexes were considered extracted from centrosymmetric dimer complexes. We performed PBE density functional (Perdew, et al., 1997) with Grimme's D3 dispersion correction (Grimme, 2004, 2006, 2011) in all calculation tasks. For Dysprosium, the CSDZ (Cundari Stevens double zeta) basis set and the corresponding pseudopotential (Cundari and Stevens, 1993; Yu, et al., 2020) was employed and the 6-311g+(d,p) basis set for other atoms like carbon, hydrogen, oxygen, nitrogen, boron sodium and chlorine. All converged wave functions are stable under the perturbations considered. The total bonding energy (BE_{total}) between fragments is defined as: $BE_{total} = E_{model} - (E_{frg1} + E_{frg2})$, where E_{model}, E_{frg1} and E_{frg2} are the energy of model complex, fragment 1 and fragment 2, respectively. The first model complex has four $B-H^{\delta-}\cdots Dy^{3+}$ interactions, and the second model

complex eight B−H$^{\delta-}$···Dy^{3+} interactions while **6Dy**'s complex has six B−H$^{\delta-}$···Na^{+} interactions. Therefore, average bonding energy (BE_{avg}) is introduced considering complexes' centrosymmetric and similarity of Dy-H and Na-H distance, namely $BE_{avg} = BE_{total} / N$ (N= 4,8,6, respectively). It is noted that we initially employed geometry optimization towards *nido*-$[C_2B_9H_{11}]^{2-}$ using the same method and basis sets before ESP calculation. All optimized structures were verified as stationary points on the potential energy surface through vibrational frequency calculations.

The related instructions and keywords we used in population analysis calculations are following: pbepbe/genecp em=gd3bj int=(ultrafine,acc2e=12) scf=qc stable=opt. The quadratically convergent SCF procedure was utilized to avoid convergence failures and the functions of the keyword "stable=opt" are to check the stability of wave function and to optimize it until stable if of instability.